Publication Nr 98/7

CHALMERS TEKNISKA HÖGSKOLA
Institutionen för Termo- och Fluiddynamik

CHALMERS UNIVERSITY OF TECHNOLOGY
Department of Thermo and Fluid Dynamics

Large-Eddy Simulation of the Flow Around a Surface-Mounted Single Cube in a Channel

by

Siniša Krajnović

Thesis for the degree of Master of Science

Göteborg, May 1998

This work was carried out at the Department of Thermo and Fluid Dynamics at CTH in collaboration with the CFD group at Volvo PV.
First, I would like to thank to my supervisor Professor Lars Davidson for his support and help in this work.
I would also like to thank to all colleagues at the CFD group at Volvo PV.
Finally, I would like to thank all the personal at the Department of Thermo and Fluid Dynamics at CTH.

Large-Eddy Simulation of the Flow Around a Surface-Mounted Single Cube in a Channel

Siniša Krajnović
Department of Thermo and Fluid Dynamics
Chalmers University of Technology

Abstract

This Master Thesis is the first part of the project "Large Eddy Simulations for Computing the Flow Around Vehicles" in collaboration between the Department of Thermo and Fluid Dynamics at CTH and the CFD group at Volvo PV. With LES we expect to be able to predict a number of physical phenomena, such as large-scale structures, unsteadiness etc. This project will give a deeper understanding of this flow and will help Volvo to optimize the flow around cars and thus to design cars in an aerodynamically better way. In the first part of the project, the flow around a surface-mounted cube is computed by using LES, in which the simple Smagorinsky model is used. Computation is performed using a finite volume code CALC-LES which is second-order accurate in space (central differencing) and time (Crank-Nicolson). A series of time-averaged resolved velocities and turbulent stresses are computed and compared with the experiments. Some global quantities such as the mean and RMS values of lift and drag coefficients, are computed. Sensitivity to grid refinement is studied.

1 Introduction

There are various approaches to numerical solution of turbulent flows. One method involves the application of Reynolds' averaging to the equations of motion to obtain the Reynolds-averaged Navier-Stokes equations (RANS). A Reynolds stress term $\overline{u_i u_j}$ that appears in RANS must be modeled to close the system of equations. That is the limitation of RANS, because the model constants are usually set by using a few simple flows which can not be applied to flows that are different from the ones used for calibration. The most straightforward approach to the numerical solution of turbulent flows is the direct numerical simulation (DNS) of turbulence, in which the governing equations are discretized and solved numerically. The problems with DNS are that one has to use higher order schemes to limit dispersion and dissipation. These schemes have little flexibility in handling complex geometries and general boundary conditions. The total cost of direct simulation is proportional to Re^3. For these reasons, there are serious limitations for use of DNS. There is also one intermediate technique between the direct simulation of turbulent flows and the solution

of the Reynolds-averaged equations, called Large-eddy simulation (LES). In LES the contribution of the large, energy-carrying structures to momentum and energy transfer is computed exactly, and only the effect of the smallest scales of turbulence is modeled.

2 Formulation of LES

Direct simulation of all scales of turbulence is feasible only at low Reynolds number, i.e. in the transitional regime, and is in principle impossible beyond some Reynolds number. This suggests a simulation technique based on some decomposition of the flow field into large-scale and small-scale structures, the first being directly simulated in three-dimensional time-dependent fashion, and the second being somehow modeled. This approach is generally called "Large - Eddy Simulation"(LES), and is introduced for the first time by Leonard [1]. The rationale for Large-Eddy Simulation is that in turbulent flow the large-scale structures, produced directly by the instability of the mean flow (shear or buoyancy effects), should be simulated directly, because 1) they are hard to model in a "universal" way, as they are highly problem-dependent and anisotropic; and 2) they are responsible for most of the transport of momentum, mass and scalars. On the other hand, the small-scale structures, produced by the energy-cascade process from larger eddies, are generally isotropic, depend little on the specific problem, and thus are much more amenable to be described by some "universal" model. Moreover, small eddies contribute little to heat and momentum transport, so that a large-eddy simulation is expected to be little sensitive to the parameterization scheme used for them [3].
The equations governing the flow and thermal fields for the incompressible flow are

$$\frac{\partial \rho}{\partial t} + \frac{\partial (\rho u_i)}{\partial x_i} = 0 \tag{1}$$

$$\frac{\partial (\rho u_i)}{\partial t} + \frac{\partial (\rho u_i u_j)}{\partial x_j} = -\frac{\partial p}{\partial x_i} + \frac{\partial}{\partial x_j} \left\{ \mu \left[\frac{\partial u_i}{\partial x_j} + \frac{\partial u_j}{\partial x_i} \right] \right\} \tag{2}$$

$$\frac{\partial (\rho T)}{\partial t} + \frac{\partial (\rho u_j T)}{\partial x_j} = \frac{\partial}{\partial x_j} \left[\Gamma \frac{\partial T}{\partial x_j} \right] + S_T \tag{3}$$

in which μ is coefficient of viscosity, Γ is the molecular thermal diffusivity, $S_T = S_H / c_p$ and S_H is a source term (power per unit volume), associated with internal heat generation.

In LES each quantity f is decomposed as

$$f = \bar{f} + f' \tag{4}$$

Decomposition Eq. 4 is the analogue of the Reynolds-decomposition of generic field into an average and a fluctuating component, which is the basis for all classical closure models of turbulence. The resolvable-scale component of f, which is still time-dependent is denoted $\bar{f}$ while f' denotes the small-scale , or subgrid (unresolved) component. The large-scale component $\bar{f}$ is the result of

applying a filtering procedure to the local and instantaneous quantities and is given by a convolution of f with a filter function $G(\vec{x})$

$$\bar{f}(\vec{x}) = \int_{\Omega} f(\vec{x}^{'}) G(\vec{x} - \vec{x}^{'}) d\vec{x}^{'} \tag{5}$$

where Ω is the entire flow domain.

In Eq. 5, f is still a continuous function defined at each point in the domain and independent of the computation grid or discretization scheme used for the numerical computation of it.

The most commonly used filter functions are the sharp Fourier cutoff filter, defined in wave space as:

$$\widehat{G}(k) = \begin{cases} 1, & \text{if } k \leq \pi/\Delta \\ 0, & \text{otherwise} \end{cases}$$

the Gaussian filter,

$$G(\vec{x}, \vec{x}^{'}) = \sqrt{(\frac{6}{\pi\Delta^2})} \exp(-\frac{6(\vec{x}-\vec{x}^{'})^2}{\Delta^2}) \ ,$$

and the top-hat filter in real space:

$$G(\vec{x}, \vec{x}^{'}) = \begin{cases} 1/\Delta, & \text{if } |\vec{x} - \vec{x}^{'}| \leq \Delta/2 \\ 0, & \text{otherwise} \end{cases}$$

Δ being the characteristic filter width. The sharp Fourier cutoff filter and the Gaussian filter are used in spectral methods and Fourier transforms. In the present work, the top-hat filter in real space is used. Applying the filtering operation given by Eq. 5 to the momentum and the continuity equations, one has the equations of motion[1]

$$\frac{\partial \rho}{\partial t} + \frac{\partial(\rho \bar{u}_i)}{\partial x_i} = 0 \tag{6}$$

$$\frac{\partial(\rho \bar{u}_i)}{\partial t} + \frac{\partial(\rho \overline{u_i u_j})}{\partial x_j} = -\frac{\partial \bar{p}}{\partial x_i} + \frac{\partial}{\partial x_j} \left\{ \mu \left[\frac{\partial \bar{u}_i}{\partial x_j} + \frac{\partial \bar{u}_j}{\partial x_i} \right] \right\} \tag{7}$$

In Eq. 7 there is the problem of filtering the product $u_i u_j$. If we decompose u_i into its resolvable-scale and subgrid-scale components, $u_i = \bar{u}_i + u_i^{'}$, then

$$\overline{u_i u_j} = \overline{\bar{u}_i \bar{u}_j} + \overline{\bar{u}_i u_j'} + \overline{u_i' \bar{u}_j} + \overline{u_i' u_j'} \tag{8}$$

This may be written

$$\overline{u_i u_j} = \bar{u}_i \bar{u}_j + L_{ij} + C_{ij} + R_{ij}, \tag{9}$$

[1]Note that by integration by parts we find that $\frac{\overline{\partial f}}{\partial x_i} = \frac{\partial \bar{f}}{\partial x_i}$.

where $L_{ij} = \overline{\bar{u}_i \bar{u}_j} - \bar{u}_i \bar{u}_j$ are the Leonard stresses, $C_{ij} = \overline{\bar{u}_i u'_j} + \overline{u'_j \bar{u}_i}$ are the cross terms, and $R_{ij} = \overline{u'_i u'_j}$ are the subgrid-scale (SGS) Reynolds stresses. The terms R_{ij}, or rather $-\rho R_{ij}$ are the analogies of the turbulent stresses arising from the RANS. The Leonard stresses represent interactions between resolved scales that result in subgrid-scales contributions. The cross terms represent interactions between resolved and unresolved scales, whereas the SGS Reynolds stresses represent interactions between small, unresolved, scales.
Due to the existence of "Leonard" and "cross" terms one has $\overline{\bar{u}_i \bar{u}_j} - \bar{u}_i \bar{u}_j \neq \overline{u'_i u'_j}$ in general. The physical reason for this inequality is that in the turbulence spectrum there is no gap between the large and the small scales, but rather a continuous "energy cascade" involving eddies of all intermediate scales [1, 2].
An alternative approach was developed by Schumann. It is suitable for finite-volume/finite-difference based computation methods and allows to drop the Leonard and cross terms. Schumann's approach consists of replacing explicit filtering by volume-averaging on each grid cell

$$\bar{f}(\vec{x}) = \frac{1}{\Delta x_1 \Delta x_2 \Delta x_3} \int_{x_1 - \frac{\Delta x_1}{2}}^{x_1 + \frac{\Delta x_1}{2}} \int_{x_2 - \frac{\Delta x_2}{2}}^{x_2 + \frac{\Delta x_2}{2}} \int_{x_3 - \frac{\Delta x_3}{2}}^{x_3 + \frac{\Delta x_3}{2}} f(\vec{x}') dx'_1 dx'_2 dx'_3 \qquad (10)$$

where x'_1, x'_2 and x'_3 are dummy variables representing x_1, x_2 and x_3, respectively, and $\Delta x_1, \Delta x_2$ and Δx_3 are the corresponding grid increments of the finite-difference/finite-volume equations [4].
After applying the over-bar operator to the velocity components u_i, one has the following important properties

$$\begin{aligned} \overline{\bar{u}_i \bar{u}_j} &= \bar{u}_i \bar{u}_j \\ \overline{u'_i \bar{u}_j} &= \overline{\bar{u}_i u'_j} = 0 \end{aligned} \qquad (11)$$

As a result of this volume-averaging on each grid cell one has the equations governing the resolved flow and thermal fields:

$$\frac{\partial \rho}{\partial t} + \frac{\partial (\rho \bar{u}_i)}{\partial x_i} = 0 \qquad (12)$$

$$\frac{\partial (\rho \bar{u}_i)}{\partial t} + \frac{\partial (\rho \bar{u}_i \bar{u}_j)}{\partial x_j} = -\frac{\partial \bar{p}}{\partial x_i} + \frac{\partial}{\partial x_j} \left\{ \mu \left[\frac{\partial \bar{u}_i}{\partial x_j} + \frac{\partial \bar{u}_j}{\partial x_i} \right] \right\} + \frac{\partial}{\partial x_j} \left(-\rho \overline{u'_i u'_j} \right) \qquad (13)$$

$$\frac{\partial (\rho \bar{T})}{\partial t} + \frac{\partial (\rho \bar{u}_j \bar{T})}{\partial x_j} = \frac{\partial}{\partial x_j} \left[\Gamma \frac{\partial \bar{T}}{\partial x_j} \right] + \frac{\partial}{\partial x_j} \left(\rho \overline{u'_j T'} \right) \qquad (14)$$

Problem with this approach is that in this procedure any large-scale quantity like $\bar{f}$ is given discontinuously (at mesh points) and because of that any quantity like $\partial \bar{f} / \partial x_i$ exists only in the sense of its finite difference representation using discrete values of $\bar{f}$ at mesh points, but not in an ordinary sense of derivatives, and one has $\frac{\overline{\partial \bar{f}}}{\partial x_i} \neq \frac{\partial \bar{f}}{\partial x_i}$ in general.
In both cases, the residual, or subgrid, stress $-\rho \overline{u'_i u'_j}$ and the residual fluxes $\rho c_p \overline{T' u'_i}$ plus eventually Leonard and cross terms, contain unresolved terms and thus have to be modeled.

A filtering approach is used in the present work.
Eq. 7 can be rewritten as

$$\begin{aligned}\frac{\partial(\rho\bar{u}_i)}{\partial t}+\frac{\partial}{\partial x_j}\left(\rho\overline{u_iu_j}\right)+\left[\frac{\partial}{\partial x_j}\left(\rho\bar{u}_i\bar{u}_j\right)-\frac{\partial}{\partial x_j}\left(\rho\overline{u_iu_j}\right)\right]=\\ -\frac{\partial\bar{p}}{\partial x_i}+\frac{\partial}{\partial x_j}\left\{\mu\left[\frac{\partial\bar{u}_i}{\partial x_j}+\frac{\partial\bar{u}_j}{\partial x_i}\right]\right\}+\left[\frac{\partial}{\partial x_j}\left(\rho\bar{u}_i\bar{u}_j\right)-\frac{\partial}{\partial x_j}\left(\rho\overline{u_iu_j}\right)\right]\end{aligned} \tag{15}$$

and using $\mu = const.$, one has

$$\begin{aligned}\frac{\partial(\rho\bar{u}_i)}{\partial t}+\frac{\partial}{\partial x_j}\left(\rho\bar{u}_i\bar{u}_j\right)=-\frac{\partial\bar{p}}{\partial x_i}+\mu\frac{\partial}{\partial x_j}\left(\frac{\partial\bar{u}_i}{\partial x_j}\right)+\mu\frac{\partial}{\partial x_i}\left(\frac{\partial\bar{u}_j}{\partial x_j}\right)\\ +\frac{\partial}{\partial x_j}\left(\rho\bar{u}_i\bar{u}_j\right)-\frac{\partial}{\partial x_j}\left(\rho\overline{u_iu_j}\right)\end{aligned} \tag{16}$$

Assuming constant density, continuity gives $\mu\frac{\partial}{\partial x_i}(\frac{\partial\bar{u}_j}{\partial x_j})=0$ and by introducing the subgrid stress tensor $\tau_{ij}=\overline{u_iu_j}-\bar{u}_i\bar{u}_j$, one has the governing equations

$$\frac{\partial\bar{u}_i}{\partial t}+\frac{\partial}{\partial x_j}\left(\bar{u}_i\bar{u}_j\right)=-\frac{1}{\rho}\frac{\partial\bar{p}}{\partial x_i}+\nu\left(\frac{\partial^2\bar{u}_i}{\partial x_j\partial x_j}\right)-\frac{\partial\tau_{ij}}{\partial x_j} \tag{17}$$

$$\frac{\partial\bar{u}_i}{\partial x_i}=0 \tag{18}$$

3 SGS Models

In an LES the equations are averaged over only small scales and retain all space-time dimensions. The averaging process is chosen to resolve numerically the physical features of interest, and the desired statistics are measured directly from the computed scales. The most important contribution of these models is to provide, or at least allow, energy transfer between the resolved and subgrid scales at roughly the correct magnitude. This transfer is usually from resolved to subgrid scales but may be reversed and the SGS model must account for reversed transfer of energy. Thus, the most important feature of a subgrid-scale model is to provide adequate dissipation in the resolved scales, where dissipation actually means transport of energy from the resolved grid scales to the unresolved subgrid scales, and the rate of dissipation in this context is actually the flux of energy through the inertial subrange.

3.1 Eddy Viscosity Models

Most subgrid scale models in use, are eddy-viscosity models, based on a gradient-diffusion hypothesis, similar to the Boussinesq hypothesis of conventional turbulence models. It consists of assuming the anisotropic part of the residual stress tensor τ_{ij} to be proportional to the resolved strain rate tensor $\bar{S}_{ij}$, i.e.

$$\tau_{ij}-\frac{1}{3}\delta_{ij}\tau_{kk}=-2\nu_T\left[\bar{S}_{ij}-\frac{1}{3}\delta_{ij}\bar{S}_{kk}\right] \tag{19}$$

in which $\bar{S}_{ij} = \frac{1}{2}[\frac{\partial \bar{u}_i}{\partial x_j} + \frac{\partial \bar{u}_j}{\partial x_i}]$, ν_T is a subgrid viscosity which has to be expressed by an model, and δ_{ij} is the Kronecker delta. If we denote the subgrid scale turbulent energy $\frac{1}{2}\frac{\tau_{kk}}{\rho}$ by the symbol k' then the left hand side of Eq. 19 can be expressed as

$$\tau_{ij} - \frac{1}{3}\delta_{ij}\tau_{kk} = \tau_{ij} - \frac{2}{3}\delta_{ij}\rho k' \tag{20}$$

Substituting Eq. 20 into Eq. 19 and this into Eq. 17 one has

$$\begin{aligned} &\frac{\partial \bar{u}_i}{\partial t} + \frac{\partial}{\partial x_j}(\bar{u}_i\bar{u}_j) = -\frac{1}{\rho}\frac{\partial \bar{p}_i}{\partial x_i} + +\nu\frac{\partial^2 \bar{u}_i}{\partial x_j \partial x_j} + \\ &\frac{\partial}{\partial x_j}\left\{-\frac{2}{3}\delta_{ij}\rho k' + \nu_T\left[\frac{\partial \bar{u}_i}{\partial x_j} + \frac{\partial \bar{u}_j}{\partial x_i} - \frac{1}{3}\delta_{ij}\frac{\partial \bar{u}_k}{\partial x_k}\right]\right\} \end{aligned} \tag{21}$$

Here is $\frac{\partial \bar{u}_k}{\partial x_k} = 0$ due to continuity.
Defining a modified pressure as

$$\bar{P} = \bar{p} + \frac{2}{3}\rho k' \tag{22}$$

one has

$$\frac{\partial \bar{u}_i}{\partial t} + \frac{\partial}{\partial x_j}(\bar{u}_i\bar{u}_j) = -\frac{1}{\rho}\frac{\partial \bar{P}}{\partial x_i} + \nu\frac{\partial^2 \bar{u}_i}{\partial x_j \partial x_j} + \frac{\partial}{\partial x_j}\left\{\nu_T\left[\frac{\partial \bar{u}_i}{\partial x_j} + \frac{\partial \bar{u}_j}{\partial x_i}\right]\right\} \tag{23}$$

In order to solve Eqs. 18 and 23 one needs a closure relation expressing ν_T as a function of resolved quantities.
All proposed subgrid models belonging to the eddy-viscosity family can be summarized under the form

$$\nu_T = clq_{sgs} \tag{24}$$

in which c is a dimensionless constant and l and q_{sgs} are a length and a velocity scale, respectively. The parameter l is generally related to the width of the filter used. In the finite difference/volume simulations, when volume-averaging approach is adopted, one express l as an average cell size, e.g. $l = \bar{\Delta} = (\Delta x_1 \Delta x_2 \Delta x_3)^{1/3}$ in which $\Delta x_i' s$ are the mesh sides. For explicit filtering approach, the formulation

$$l = \bar{\Delta} = (\Delta_1 \Delta_2 \Delta_3)^{1/3} \tag{25}$$

is used. Here $\Delta_i' s$ are filter widths along the three directions.

3.2 Smagorinsky model

The Smagorinsky model is the most popular eddy-viscosity model. It is based on the equilibrium hypothesis

$$-\tau_{ij}\bar{S}_{ij} = \epsilon_v \tag{26}$$

in which ϵ_v is the viscous dissipation of SGS energy and $\tau_{ij}\bar{S}_{ij} = \epsilon_{sgs}$ is minus production of SGS energy. The equilibrium assumption is based on the

consideration that the small scales of motion have shorter time scales than the large, energy-carrying eddies. The equilibrium assumption implies inertial range dynamics, i.e. energy is generated at the large-scale level, and transmitted to smaller and smaller scales, where the viscous dissipation takes place.
If the viscous dissipation is modeled as $\epsilon_v \sim \frac{q_{sgs}^3}{l}$, and Eq. 19 is substituted into Eq. 26, one has

$$2\nu_T \bar{S}_{ij} \bar{S}_{ij} \sim \frac{q_{sgs}^3}{l} \tag{27}$$

With Eq. 24 one obtains from Eq. 27 that

$$q_{sgs} \sim l|\bar{S}| \tag{28}$$

where $|\bar{S}| = (2\bar{S}_{ij}\bar{S}_{ij})^{1/2}$. Now, by using Eq. 25 the eddy viscosity can be written

$$\nu_T = (C_s\bar{\Delta})^2|\bar{S}| \tag{29}$$

Since the Smagorinsky constant C_s is real, the model is absolutely dissipative, i.e.

$$\epsilon_{sgs} = -(C_s\bar{\Delta})^2|\bar{S}|^3 \leq 0 \tag{30}$$

Eq. 30 can easily be derived in the following way:

$$\begin{aligned} \epsilon_{sgs} = -\epsilon_v \sim -\frac{q_{sgs}^3}{l} \sim \tau_{ij}\bar{S}_{ij} = -2\nu_T \bar{S}_{ij}\bar{S}_{ij} = \\ -2(C_s\bar{\Delta})^2|\bar{S}|\bar{S}_{ij}\bar{S}_{ij} = -(C_s\bar{\Delta})^2|\bar{S}|^3 \end{aligned} \tag{31}$$

In the present work the value of $C_s = 0.1$ is used.
The Smagorinsky model assumes that the main function of subgrid scales is to remove energy from the large scales and dissipate it through the action of viscous forces. On the average, energy is transferred from the large to the small scales ("forward scatter") but reversed energy flow ("backscatter") from the small scales to the large ones, associated with random fluctuations of the subgrid-scale stresses may also occur. As discussed by Piomelli [10] the net energy transfer from large to small scales is given by the subgrid dissipation from Eq. 26. From Eq. 30 follows that Smagorinsky model is absolutely dissipative, i.e. it cannot predict backscatter.
In his attempt to overcome this problem Germano [5] developed the dynamic SGS model.

3.3 Near-wall damping

When using the Smagorinsky model, the wall region deserves special treatment. The SGS model has to account for the fact that the resolved strain rate does not vanish on the walls, while the subgrid scale stress does. Therefore, the subgrid viscosity ν_T must vanish at the walls. This is due the fact that on solid walls the large eddies dissipate their energy directly rather than by the usual "energy cascade" involving smaller and smaller eddies. Wall effects can be partially

taken into account by appropriately "damping" the length scale l near to the walls.
An approach is to use the van Driest damping function

$$f\left(\frac{l}{l_\infty}\right) = 1 - \exp\left(-\frac{y^+}{A^+}\right) \tag{32}$$

in which l_∞ is the value of l far from walls, y^+ is the distance from the nearest wall, given as $y^+ = \frac{y u_*}{\nu}$ and A^+ is a constant for which the value of 25 is generally used.
The alternative form of the damping function from Eq. 32 is

$$f = 1 - \exp\left[-\left(\frac{y^+}{A^+}\right)^2\right] \tag{33}$$

The van Driest damping functions in Eqs. 32 and 32 have the property that $l = 0$ on the wall. Some researchers use van Driest Damping function [6] of the form

$$f = \left[1 - \exp\left(-\frac{y^+}{A^+}\right)^a\right]^b \tag{34}$$

with rather arbitrary constants a and b. Taking near-wall damping into account, the Smagorinsky SGS model for ν_T from Eq. 29 can be rewritten as

$$\nu_T = (C_s f \bar{\Delta})^2 |\bar{S}| \tag{35}$$

in which f is given by one of the expressions in Eqs. 32, 33 or 34.

3.4 The Dynamic SGS model (DSM)

In DSM the model coefficient is computed dynamically as the calculation progress rather than being determined a priori.
Germano introduced two filters: the grid filter denoted by $\bar{G}$ with filter width $\bar{\Delta}$, which defines the resolved and subgrid scales, and the test filter denoted by $\hat{G}$ with filter width $\hat{\Delta}$. Here is $\hat{\Delta} > \bar{\Delta}$ (usually $\hat{\Delta} = 2\bar{\Delta}$) and

$$\bar{f}(\vec{x}) = \int f(\vec{x}')\bar{G}(\vec{x} - \vec{x}')d\vec{x}' \tag{36}$$

$$\hat{f}(\vec{x}) = \int f(\vec{x}')\hat{G}(\vec{x} - \vec{x}')d\vec{x}' \tag{37}$$

By applying $\hat{G}$ to the equation of motion (Eq. 17) one has

$$\frac{\partial \widehat{\bar{u}_i}}{\partial t} + \frac{\partial}{\partial x_j}\left(\widehat{\bar{u}_i \bar{u}_j}\right) = -\frac{1}{\rho}\frac{\partial \widehat{\bar{p}}}{\partial x_i} + \nu\left(\frac{\partial^2 \widehat{\bar{u}_i}}{\partial x_j \partial x_j}\right) - \frac{\partial \widehat{\tau}_{ij}}{\partial x_j} \tag{38}$$

Here is

$$\widehat{\tau}_{ij} = \widehat{\bar{u}_i \bar{u}_j} - \widehat{\bar{u}_i}\widehat{\bar{u}_j} \tag{39}$$

Substituting Eq. 39 into Eq. 38 and adding $-\frac{\partial}{\partial x_j}(L_{ij}) = -\frac{\partial}{\partial x_j}\left\{\widehat{\bar{u}_i}\widehat{\bar{u}_j} - \widehat{\bar{u}_i\bar{u}_j}\right\}$ to both sides one has

$$\frac{\partial \widehat{\bar{u}}_i}{\partial t} + \frac{\partial}{\partial x_j}\left(\widehat{\bar{u}}_i\widehat{\bar{u}}_j\right) = -\frac{1}{\rho}\frac{\partial \widehat{\bar{p}}}{\partial x_i} + \nu\left(\frac{\partial^2 \widehat{\bar{u}}_i}{\partial x_j \partial x_j}\right) - \frac{\partial}{\partial x_j}\left\{\widehat{\bar{u}_i\bar{u}_j} - \widehat{\bar{u}}_i\widehat{\bar{u}}_j\right\} \tag{40}$$

By introducing the SGS stress on the test level

$$T_{ij} = \widehat{\bar{u}_i\bar{u}_j} - \widehat{\bar{u}}_i\widehat{\bar{u}}_j \tag{41}$$

Eq. 40 becomes

$$\frac{\partial \widehat{\bar{u}}_i}{\partial t} + \frac{\partial}{\partial x_j}\left(\widehat{\bar{u}}_i\widehat{\bar{u}}_j\right) = -\frac{1}{\rho}\frac{\partial \widehat{\bar{p}}}{\partial x_i} + \nu\left(\frac{\partial^2 \widehat{\bar{u}}_i}{\partial x_j \partial x_j}\right) - \frac{\partial T_{ij}}{\partial x_j} \tag{42}$$

$L_{ij} = \widehat{\bar{u}_i\bar{u}_j} - \widehat{\bar{u}}_i\widehat{\bar{u}}_j$ is called the resolved turbulent stress. The resolved turbulent stresses are Reynolds stresses by the scales whose length is intermediate between the grid filter width and the test filter width, i.e. the small resolved scales. The dynamic Leonard stresses

$$L_{ij} = T_{ij} - \widehat{\tau}_{ij} \tag{43}$$

relate the resolved turbulent stress L_{ij}, which can be calculated explicitly, to the SGS stresses at the test and grid levels, T_{ij} and τ_{ij}. The subgrid scale stresses can be parameterized by eddy viscosity models of the form (Eq. 29)

$$\tau_{ij} - \frac{\delta_{ij}}{3}\tau_{kk} = -2C\bar{\Delta}^2|\bar{S}|\bar{S}_{ij} \tag{44}$$

$$T_{ij} - \frac{\delta_{ij}}{3}T_{kk} = -2C\hat{\Delta}^2|\widehat{\bar{S}}|\widehat{\bar{S}}_{ij} \tag{45}$$

By introducing $\beta_{ij} = \bar{\Delta}^2|\bar{S}|\bar{S}_{ij}$ and $\alpha_{ij} = \hat{\Delta}^2|\widehat{\bar{S}}|\widehat{\bar{S}}_{ij}$ and substituting Eq. 44 and 45 into 43 one has

$$L^a_{ij} = L_{ij} - \frac{\delta_{ij}}{3}L_{kk} = -2C\alpha_{ij} + 2\widehat{C\beta_{ij}} \tag{46}$$

in which L^a_{ij} is the anisotropic part of the SGS stress at the test level. To obtain a single coefficient from these five independent equation, Lilly proposed to minimize the sum of the squares of the residual E_{ij} given as

$$E_{ij} = L^a_{ij} + 2CL_{ij} - 2C\widehat{\beta}_{ij} \tag{47}$$

by multiplying both sides of Eq. 46 with $\alpha_{ij} - \widehat{\beta}_{ij}$ to yield

$$C(\vec{x},t) = -\frac{1}{2}\frac{L^a_{ij}(\alpha_{ij} - \widehat{\beta}_{ij})}{(\alpha_{mn} - \widehat{\beta}_{mn})(\alpha_{mn} - \widehat{\beta}_{mn})} \tag{48}$$

C is usually assumed to be only a function of time and of the spatial coordinates in inhomogeneous directions. The dynamic model has problems with negative values of the C-coefficient, because negative C (negative diffusion) causes numerical problems. In his attempt to improve the dynamic model Ghosal [7] tried to optimize the equation for C globally, but still with the constraint that $C > 0$. This optimization gave an Fredholm's integral equation of the second kind which is very expensive to solve. Davidson presented [8] a dynamic one-equation subgrid model. An modification of this model given in [9] will be used in the future work.

4 The Test Case

The case that was selected for simulation in this work was the flow around a surface-mounted cubical obstacle placed on a channel wall for which the measurements were taken from the work of Martinuzzi (1992) and Martinuzzi and Tropea (1993). A surface-mounted cube has been one of the test cases of the "Workshop on LES of Flows past Bluff Bodies", Rotach-Egern, Tegernsee, June 26-28 1995 and 6th ERCOFTAC/IAHR/COST Workshop on Refined Flow Modeling, Delft University of Technology, June 1997.
The geometry of the computational domain is given in Fig. 1.
For the simulations a domain with an upstream length of $\frac{x_1}{H} = 3$ and a downstream length of $\frac{x_2}{H} = 6$ was used, while the span-wise width was set to $\frac{b}{H} = 7$. The Reynolds number based on the incoming mean bulk velocity U_b and the obstacle height H is 40000, while based on the channel height h, it is 80000. Even if the geometry of the flow configuration is rather simple, physically the flow is quite complex with multiple separation regions and vortices.

4.1 Boundary Conditions

The following boundary conditions were used: One-seventh-power profile was used at the inlet. The lateral boundaries were treated as slip surfaces. At the downstream boundary, convective boundary condition $\frac{\partial u_i}{\partial t} + c\frac{\partial u_i}{\partial x} = 0$ was used. Here c is the mean bulk velocity U_b. At the upper and lower surfaces the no-slip conditions were used.

4.2 Subgrid-Scale Model

The standard Smagorinsky model with van Driest damping from Eq. 34 with $a = b = 1$, near solid walls was implemented in the present work. In the future work, one-equation model of Davidson will be studied.

4.3 Computational Grid and Numerical Details

The measurements for the flow were available and Cartesian coordinate systems were used, so that grid was generated easily. Four different grids were used in the calculation, and they are given in Table 1.. A grid stretching was employed in the region around the cube and near to the walls, while a uniform grid distribution with cell size Δ_i $(i = x, z)$ was used in the region far from the body [13]. The geometric sequence was used for stretching the cell size between δ_i $(i = x, z)$ and Δ_i $(i = x, z)$ or in y-direction, between δ_y and $\delta_{y,max}$. Here, δ_i $(i = x, z)$ is the distance from the cube surface to the nearest node in x and z-direction, while δ_y is the distance from the cube surface to the nearest node, or from the wall to the nearest node in y-direction. The values of Δ_i $(i = x, z)$ and δ_i $(i = x, y, z)$ are given in Table 1. For time advancing, a constant time step Δt was used and is given in Table 1. The residual source criterion of the form $R = \sum_{allnodes} |\alpha \sum_{nb} a_{nb}(\bar{u}_i)_{nb}^{n+1} + b - a_P(\bar{u}_i)_P^{n+1}|$ was used at each time step with the convergence criterion set to 0.001 in all calculations. The inlet conditions were specified to contain 4 percent turbulence. Initial conditions were fluid at rest or $U = 1$, $V = 0$ and $W = 0$ in the hole computational domain.

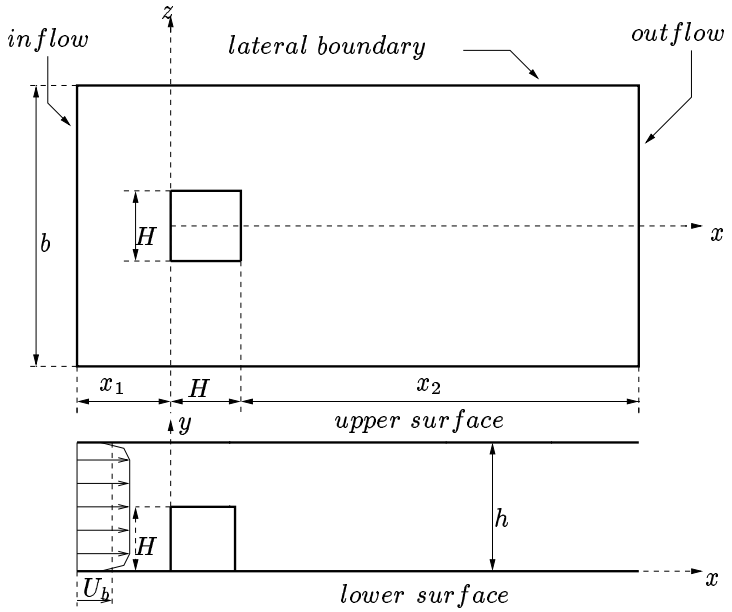

Figure 1: Geometry of the test.

Mesh	$Nodes$	Δ_x	Δ_z	δ_x	δ_y	δ_z	Δt	$T_{averaging}$
A	$80 \times 48 \times 72$	0.20	0.20	0.0481	0.0207	0.0240	0.04	150
B	$160 \times 48 \times 80$	0.20	0.20	0.0118	0.0207	0.0158	0.03	112.5
C	$160 \times 48 \times 72$	0.20	0.20	0.0118	0.0207	0.0204	0.01	150
D	$160 \times 48 \times 144$	0.20	0.20	0.0118	0.0207	0.0013	0.01	35

Table 1: Geometrical and numerical details of the meshes.

5 Description of Numerical Methodology

5.1 General description

Calculation performed with the CALC-LES code are presented. The code CALC-LES is based on a 3-D finite-volume method for solving the incompressible Navier-Stokes equations employing a non-staggered, cell-size grid arrangement. Both convective and viscous fluxes are approximated by central differences of second order accuracy. A Crank-Nicolson second-order scheme has been used for time integration. The momentum equations are solved with Gauss-Seidel method whereas a multigrid V-cycle is used for the acceleration of convergence when solving the pressure equations.

5.2 The Method

CALC-LES employs an implicit, two-step time-advancement method. Integration of the filtered Navier-Stokes Eq. 23 over a time interval from t to $t+\Delta t$ and over the control volume gives

$$\begin{aligned}\int_t^{t+\Delta t}\int_{CV}\frac{\partial \bar{u}_i}{\partial t}dtdV+\int_t^{t+\Delta t}\int_{CV}\frac{\partial}{\partial x_j}\left(\bar{u}_i\bar{u}_j\right)dtdV=\\ -\int_t^{t+\Delta t}\int_{CV}\frac{1}{\rho}\frac{\partial \bar{P}}{\partial x_i}dtdV+\int_t^{t+\Delta t}\int_{CV}\nu\frac{\partial^2\bar{u}_i}{\partial x_j\partial x_j}dtdV\\ -\int_t^{t+\Delta t}\int_{CV}\frac{\partial \tau_{ij}}{\partial x_j}dtdV\end{aligned} \tag{49}$$

This may be discretized as

$$\begin{aligned}\frac{\bar{u}_i^{n+1}-\bar{u}_i^n}{\Delta t}=-\alpha\frac{\partial}{\partial x_j}\left(\bar{u}_i^{n+1}\bar{u}_j^{n+1}\right)-(1-\alpha)\frac{\partial}{\partial x_j}\left(\bar{u}_i^{n}\bar{u}_j^{n+1}\right)+\\ \alpha\nu\frac{\partial^2\bar{u}_i^{n+1}}{\partial x_j\partial x_j}+(1-\alpha)\nu\frac{\partial^2\bar{u}_i^{n}}{\partial x_j\partial x_j}-\alpha\frac{\partial\tau_{ij}^{n+1}}{\partial x_j}+\\ (1-\alpha)\frac{\partial\tau_{ij}^{n}}{\partial x_j}-\frac{\alpha}{\rho}\frac{\partial\bar{P}^{n+1}}{\partial x_i}-\frac{(1-\alpha)}{\rho}\frac{\partial\bar{P}^{n}}{\partial x_i}\end{aligned} \tag{50}$$

to give

$$\bar{u}_i^{n+1}=\bar{u}_i^n+\Delta tH(\bar{u}_i^n,\bar{u}_i^{n+1})-\frac{1}{\rho}\alpha\Delta t\frac{\partial\bar{P}^{n+1}}{\partial x_i}-\frac{1}{\rho}(1-\alpha)\Delta t\frac{\partial\bar{P}^{n}}{\partial x_i} \tag{51}$$

where

$$\begin{aligned}H(\bar{u}_i^n,\bar{u}_i^{n+1})=-\alpha\frac{\partial}{\partial x_j}\left(\bar{u}_i^{n+1}\bar{u}_j^{n+1}\right)-(1-\alpha)\frac{\partial}{\partial x_j}\left(\bar{u}_i^{n}\bar{u}_j^{n+1}\right)+\\ \alpha\nu\frac{\partial^2\bar{u}_i^{n+1}}{\partial x_j\partial x_j}+(1-\alpha)\nu\frac{\partial^2\bar{u}_i^{n}}{\partial x_j\partial x_j}-\alpha\frac{\partial\tau_{ij}^{n+1}}{\partial x_j}+(1-\alpha)\frac{\partial\tau_{ij}^{n}}{\partial x_j}\end{aligned} \tag{52}$$

The Crank-Nicolson method results from setting $\alpha = 0.5$ in Eq. 51. In the present work $\alpha = 0.6$ was used. The standard form of control volume formulation of Eq. 51 is

$$a_P(\bar{u}_i)_P^{n+1}=\alpha\sum a_{nb}(\bar{u}_i)_{nb}^{n+1}+b \tag{53}$$

where $i = 1, 2, 3$ and

$$b = (1-\alpha)\sum a_{nb}(\bar{u}_i)^n_{nb} + (a^o_P - (1-\alpha)\sum a_{nb})(\bar{u}_i)^n_P + S$$

$$a_P = a^o_P + \alpha \sum a_{nb}$$

$$a^o_P = \frac{\Delta V}{\Delta t}$$

The source term S includes the pressure terms and one part of the subgrid stresses given by $\frac{\partial}{\partial x_j}(\nu_T \frac{\partial \bar{u}_j}{\partial x_i})$. Eq. 53 can now be solved to give $\bar{u}_i^{n+1}$ which does not satisfy continuity. An intermediate velocity field $\bar{u}_i^*$ is computed by subtracting the implicit part of the pressure gradient term, i.e, $\frac{\alpha}{\rho}\frac{\partial \bar{p}^{n+1}}{\partial x_i}$

$$\bar{u}_i^* = \bar{u}_i^{n+1} + \frac{\alpha}{\rho}\frac{\partial \bar{P}^{n+1}}{\partial x_i} \tag{54}$$

We take the divergence of Eq. 54 requiring that continuity equation for the face velocities should be satisfied at time step $n+1$, i.e $\frac{\partial \bar{u}^{n+1}_{i,face}}{\partial x_i} = 0$ to obtain

$$\frac{\partial \bar{P}^{n+1}}{\partial x_i \partial x_i} = \frac{\rho}{\Delta t \alpha}\frac{\partial \bar{u}^*_{i,face}}{\partial x_i} \tag{55}$$

The face velocities $\bar{u}_{i,face}$ are obtained by linear interpolation.

The numerical algorithm is given by:

1. Solve the discretized Navier-Stokes Eq. 53.
2. Create an intermediate velocity field $\bar{u}^*_{i,face}$ given in Eq. 54
3. Solve the Poisson equation 55.
4. Compute the face velocities, which satisfy continuity, as

$$\bar{u}^{n+1}_{i,face} = \bar{u}^*_{i,face} + \frac{\alpha}{\rho}\left(\frac{\partial \bar{P}^{n+1}}{\partial x_i}\right)_{face} \tag{56}$$

5. Repeat steps 1 to 4 till convergence is reached.
6. Compute the turbulent viscosity ν_T.
7. Next time step.

5.3 Computing time

CALC-LES has recently been parallelized by Silicon Graphics [14] and all computations were done on the 64-processors ORIGIN 2000 (recently installed at Chalmers). A typical CPU time per iteration on four processors on a mesh with 600000 nodes was 12 sec and the number of iterations per time step is 3 or 4. Even if the pressure equations is solved with en efficient multigrid method, solving of the pressure equations is still very expensive. Time per iteration and number of iterations for each time step are given in Table 2.

Mesh	N_{CPU}	$T_{iteration}$	$N_{iteration}$
A	1	8.61	2
B	4	12.15	4
C	4	10.94	3-4
D	4	24.89	3

Table 2: Time per iteration $T_{iteration}$ in seconds and number of iterations $N_{iteration}$.

6 Some results

The flow around a surface-mounted cube contains almost no statistically equivalent points over which the results can be averaged. Because of the inability to average over statistically equivalent points, the symmetry was used as a measure of whether the simulation has been run long enough. The averaging times in the simulation varied between $35H/U$ and $150H/U$ where H is the cube height and U is the bulk velocity at the inlet. All computations were started with uniform inlet velocity which was changed to one-seventh-power profile after 500 time steps. The reason for doing this is that the pressure solutions were unstable when computations were started with one-seventh-power profile. In this work some global quantities, such as mean and RMS lift and drag coefficients were computed. A time-averaged resolved velocities and turbulent stresses were computed and compared with experimental results. In the case of $u'v'$, both resolved quantity $\langle\overline{u'v'}\rangle_t$ and the SGS quantity $\langle\tau_{12}\rangle_t$ were computed as suggested by Reynolds [11], while for other quantities the SGS quantities were impossible to compute and only the resolved quantities were compared with the experiments. Here $\langle.\rangle_t$ denotes time-average.
All time-averaged velocities and stresses are compared with the experiments only for the values $z = 0$ and $z = 1$. They are shown in Fig. 12 to Fig. 57. All cases gave very similar results for almost all time-averaged velocities and turbulent stresses. Mean velocity profile $\langle\bar{u}\rangle_t$ was disturbed for $x = -1.0$ and $z = 0.0$ as it is shown in Figs., 12, 13, 34, 46. This is probably due to bad mesh in that part of the domain. $\langle\bar{u}\rangle_t$ became better with the grid refinement for $x = 0.5$ and $x = 1.0$. This improvement is not noticed in the region behind the cube. Mean velocity profile $\langle\bar{v}\rangle_t$ for $x = 1.0$,$z = 0.0$ is given in Figs. 17, 18, 36 and 48 both for the node before the surface and for the node after the surface. This is done because there are no nodes on the surface of the cube.
Generally the results for the velocities are in much better agreement with the experiment than the results for the stresses. The author has concluded from the comparison between resolved mean turbulent stress $\langle\overline{u'v'}\rangle_t$ and real turbulent stress $\langle\overline{u'v'}\rangle_t + \langle\tau_{12}\rangle_t$ that the difference between them is almost negligible.
All results were compared with the results of both Workshops. The author has found that the results from this work are very similar to the results of H. Wengle from Univ. der Bundeswehr Munchen, Germany.

Mesh	C_L	$C_{L,rms}$	C_D	$C_{D,rms}$	CFL_x	CFL_y	CFL_z
A	0.5178	0.0244	0.6371	0.0420	1.55	2.54	2.23
B	0.5366	0.0260	0.5593	0.0379	7.99	2.92	4.80
C	0.5264	0.0557	0.5717	0.0859	6.82	3.36	2.93
D	-	-	-	-	6.00	3.56	42.51

Table 3: Mean and RMS values of lift and drag coefficients and CFL values.

6.1 Global Quantities and Numerical Stability

The convection Courant Number defined as $CFL_i = \frac{u_i \Delta t}{\Delta x_i}$, $(i = x, y, z)$ is computed at the end of each calculation, and maximum values are given in Table 3.

The author has found that the regions with largest CFL values are located in the front of the cube, at the nodes closest to the surface. Only a small part of the domain has that high values of CFL. Even few nodes with high CFL can make convergence very bad. In the case D the value of CFL in z-direction is equal to 42.51 which caused divergence. The author has noticed that refinement of the mesh in the z-direction increases CFL much faster than refinement of the mesh in the x-direction.

Calculation for the case A was run on 1 CPU while for the cases B,C and D, 4 CPUs were used. It is obvious that high CFL values make calculation unstable. The mean and RMS values of the time averaged drag and lift coefficients are given in Table 3, and the time history of C_D and C_L is given in Figs. 2, 3, 4, 5, 6, 7. There are no experimental values for drag and lift coefficients known to the author. The values of mean and RMS values for cases A and B are very similar. There is a big difference in RMS values between cases A and C and between cases B and C. Drag and lift coefficients for the case D are not reliable (calculation crashed) and are not given in this paper.

The case studied in this paper was a test case at 6th ERCOFTAC/IAHR/COST Workshop on Refined Flow Modelling in Delft (1997), using RANS Models. The velocity profiles, especially further downstream of the cube, are much better predicted by LES in the present work. The turbulence stresses are in significantly better agreement with the experimental values. For this superiority of LES, high price has to be paid. The surface streamlines on the floor of the channel for the cases A and C are shown in Fig. 8 and 9. The author has found a slight lack of symmetry in the right part of both figures. This is an indication that these simulations have not been run long enough. In Fig. 10 isosurface of the velocity and isosurface of the pressure are shown. The main features of the flow around small aspect ratio obstacles are shown in schematic form in Fig. 11 [12]. The author has found very good agreement between Figs. 10 and 11.

6.2 Conclusions

A refinement of the mesh does not automatically produce better results. Only refinements in x-direction and z-direction were done in the present work. It is possible that the refinement in the y-direction should give some improvement in the accuracy.

It is very difficult to study sensitivity to grid refinement because refining the grid change also the model. This is because $\bar{\Delta}$ in $\nu_T = (C_s \bar{\Delta})^2 |\bar{S}|$ is defined as

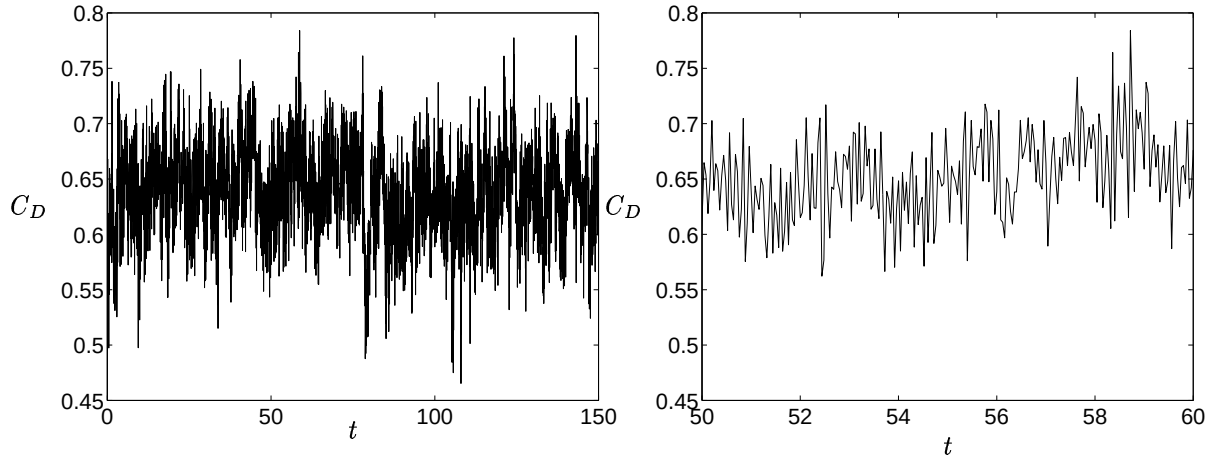

Figure 2: Time history for C_D. Mesh A.

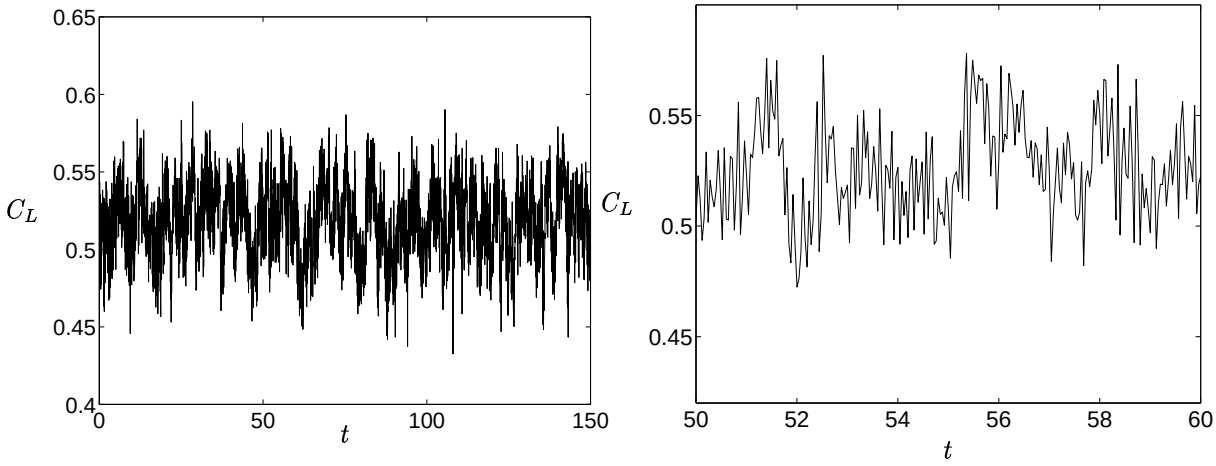

Figure 3: Time history for C_L. Mesh A.

$\bar{\Delta} = (\Delta_1 \Delta_2 \Delta_3)^{1/3}$. It is possible to define $\bar{\Delta}$ so that it is mesh independent but this should increase the cost of the calculation.

It is well-known that boundary conditions can affect the solution within a domain if the domain is too small. The author didn't find any indication that this is the case in the present work.

In the present work one-seventh-power profile was used at the inlet. The author has found very poor agreement with experiments near the inlet. The fully developed channel flow at the inlet will be used in the future work, because that is the only proper inflow condition.

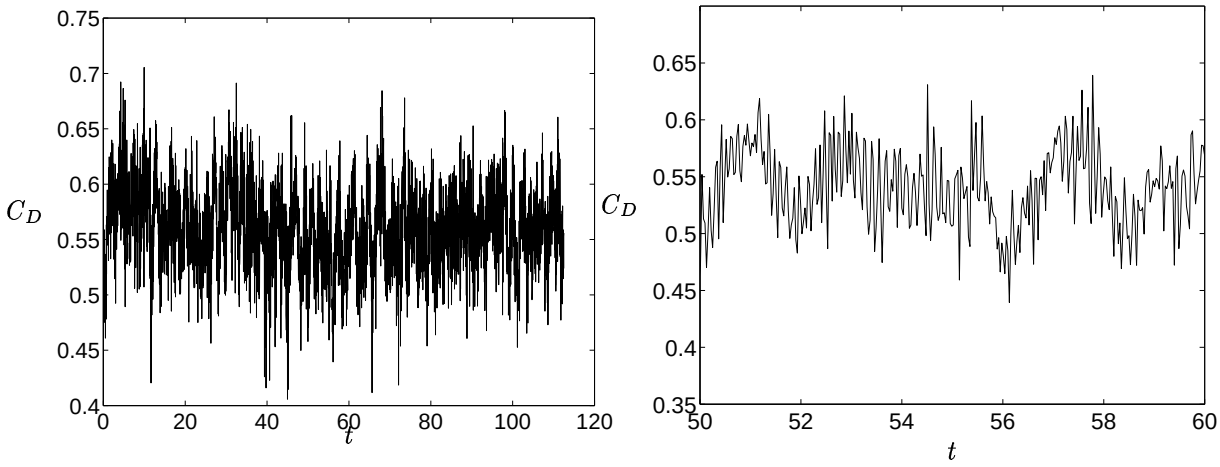

Figure 4: Time history for C_D. Mesh B.

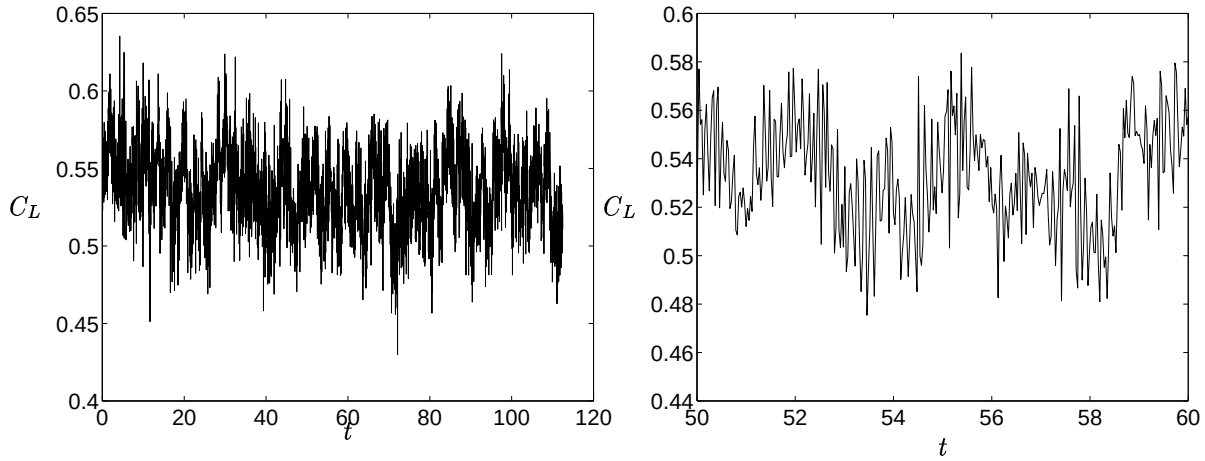

Figure 5: Time history for C_L. Mesh B.

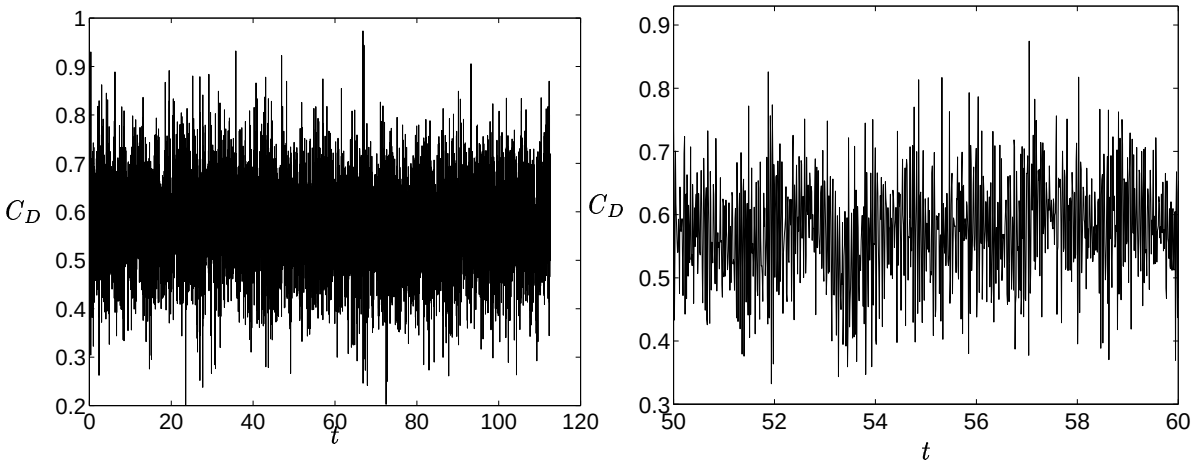

Figure 6: Time history for C_D. Mesh C.

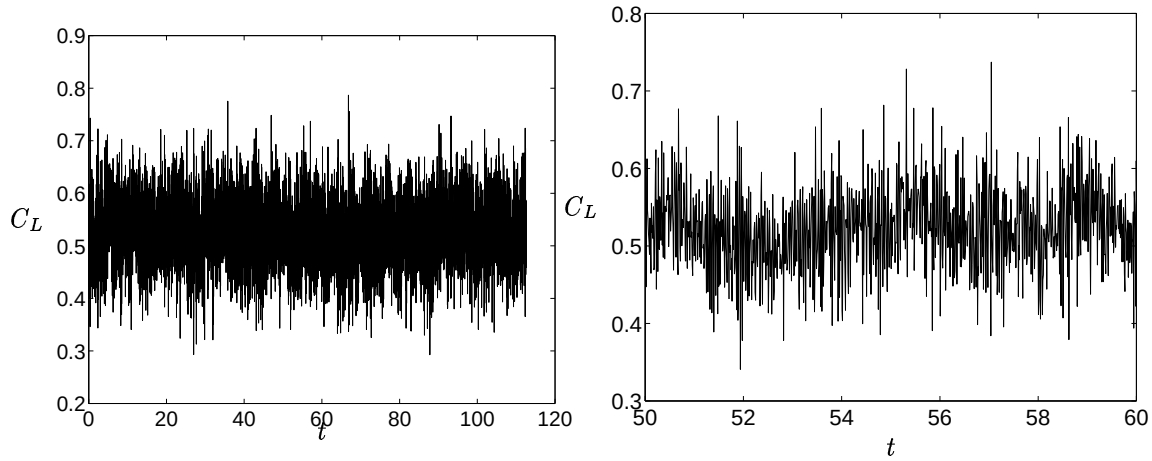

Figure 7: Time history for C_L. Mesh C.

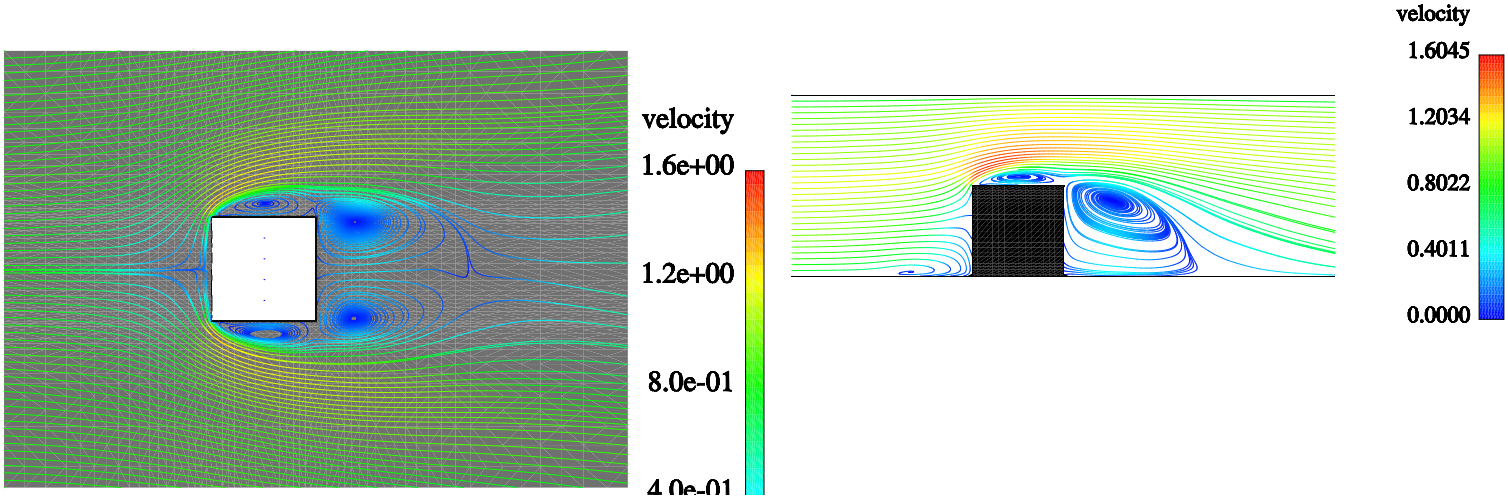

Figure 8: Time-averaged streamlines of the mean flow projected onto the floor of the channel (left) and time-averaged streamlines of the mean flow projected onto the centerline (right). Mesh A.

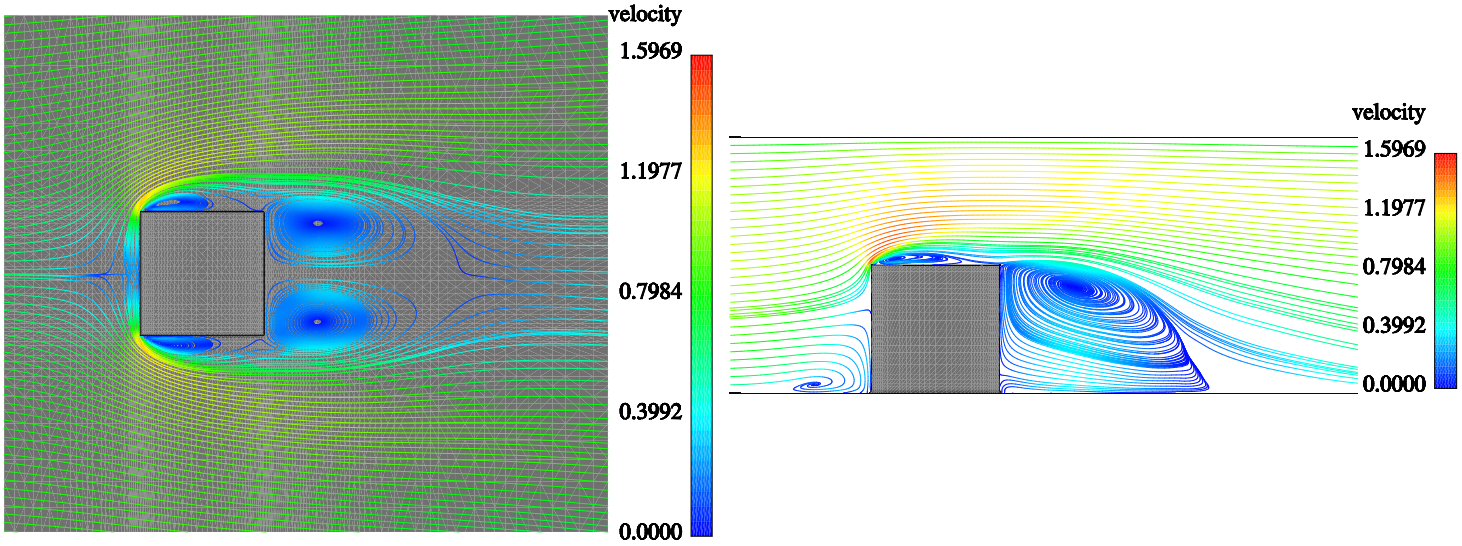

Figure 9: Time-averaged streamlines of the mean flow projected onto the floor of the channel (left) and time-averaged streamlines of the mean flow projected onto the centerline (right). Mesh C.

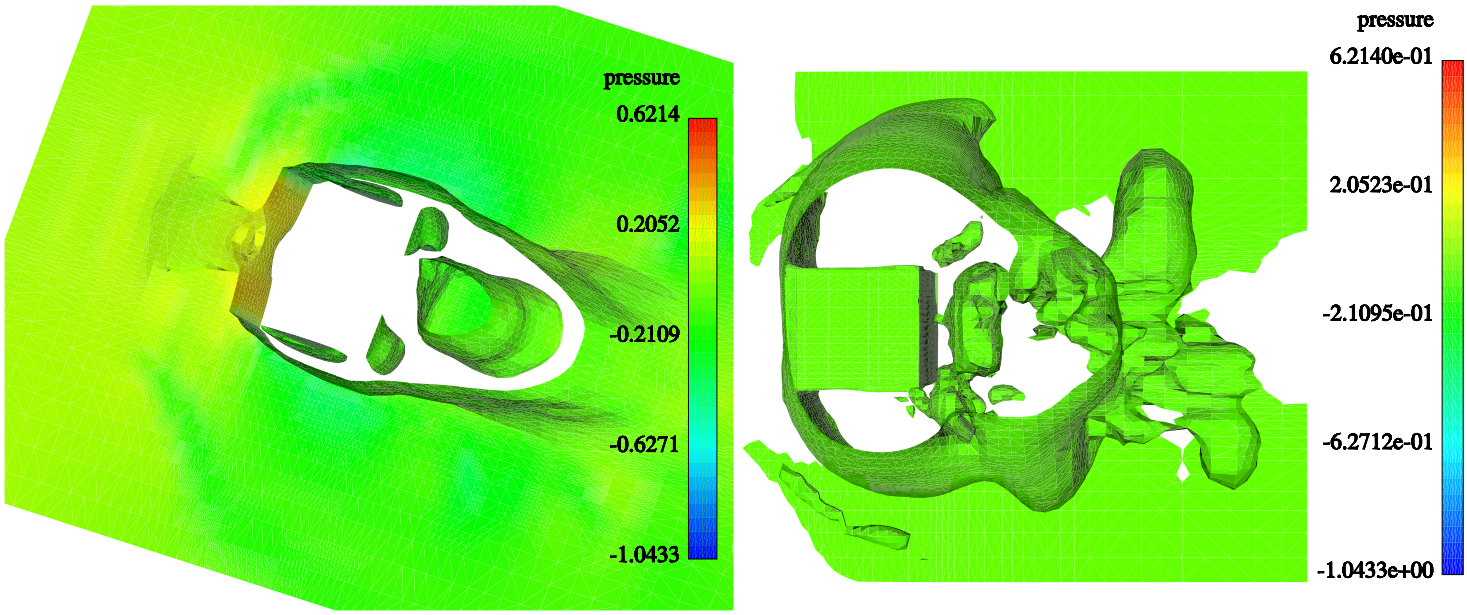

Figure 10: Isosurface of the time-averaged velocity coloured with pressure (left) and isosurface of the instantaneous pressure (right). Mesh A. In the case of the velocity the section plane was made at $y = 0.5$ and in the case of the pressure the section plane was made at $y = 1.5$.

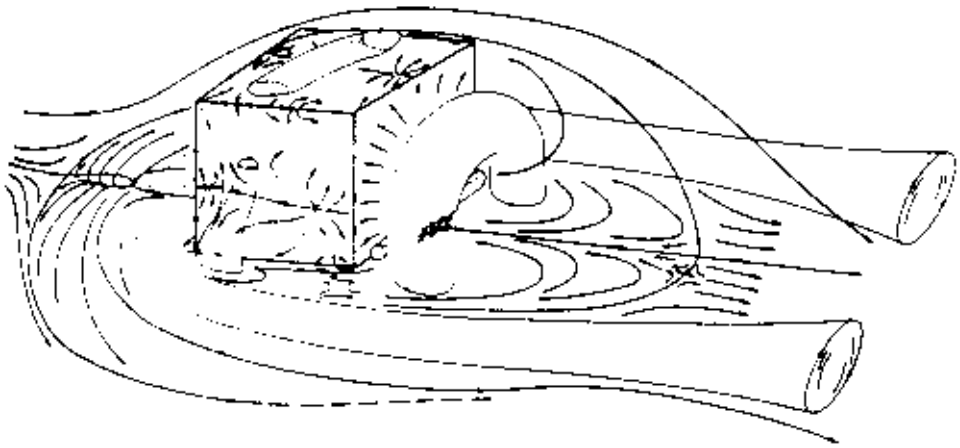

Figure 11: Schematic representation of the flow around a surface-mounted cube.

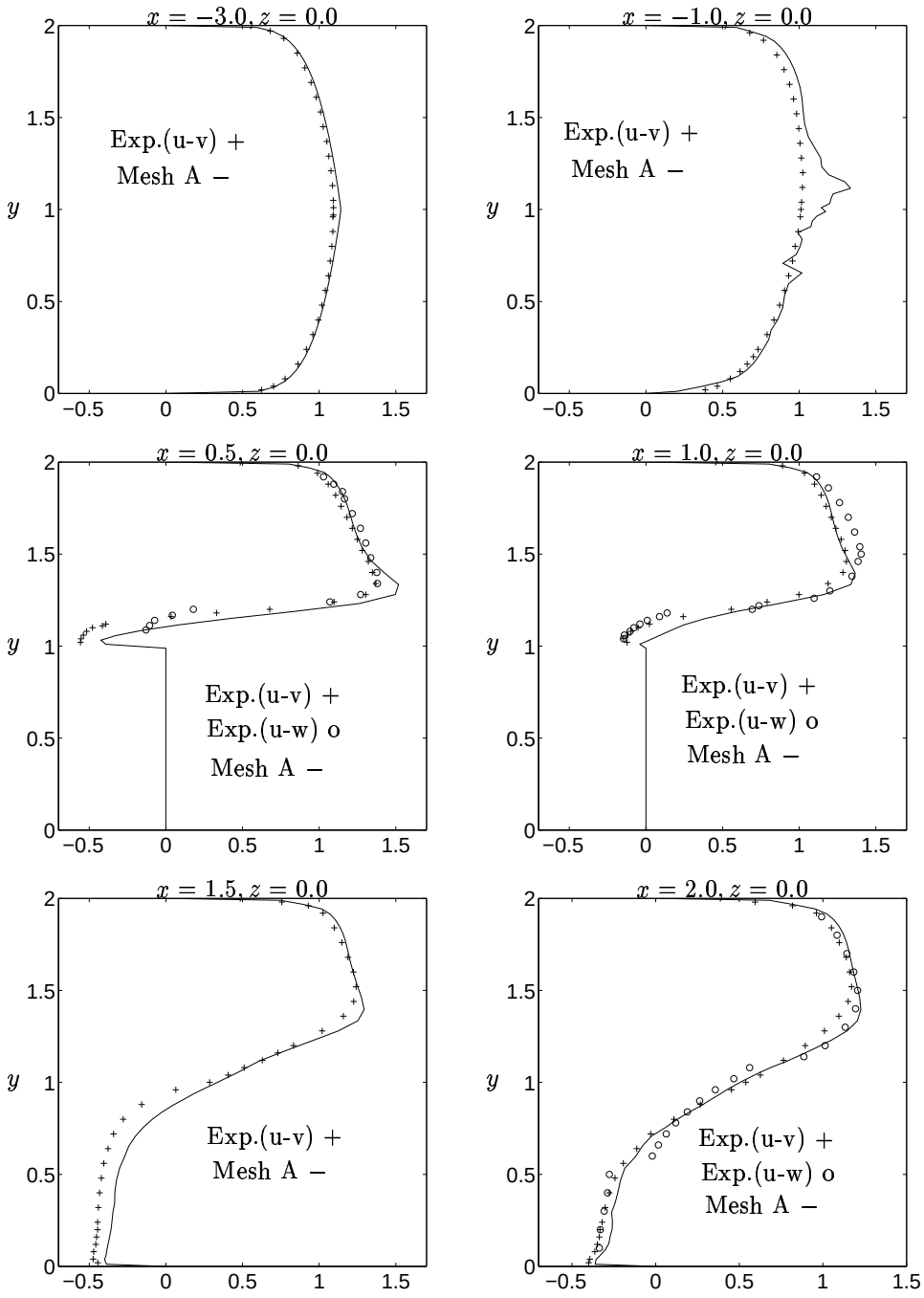

Figure 12: Mean velocity profile $\langle \bar{u} \rangle_t$. Mesh A.

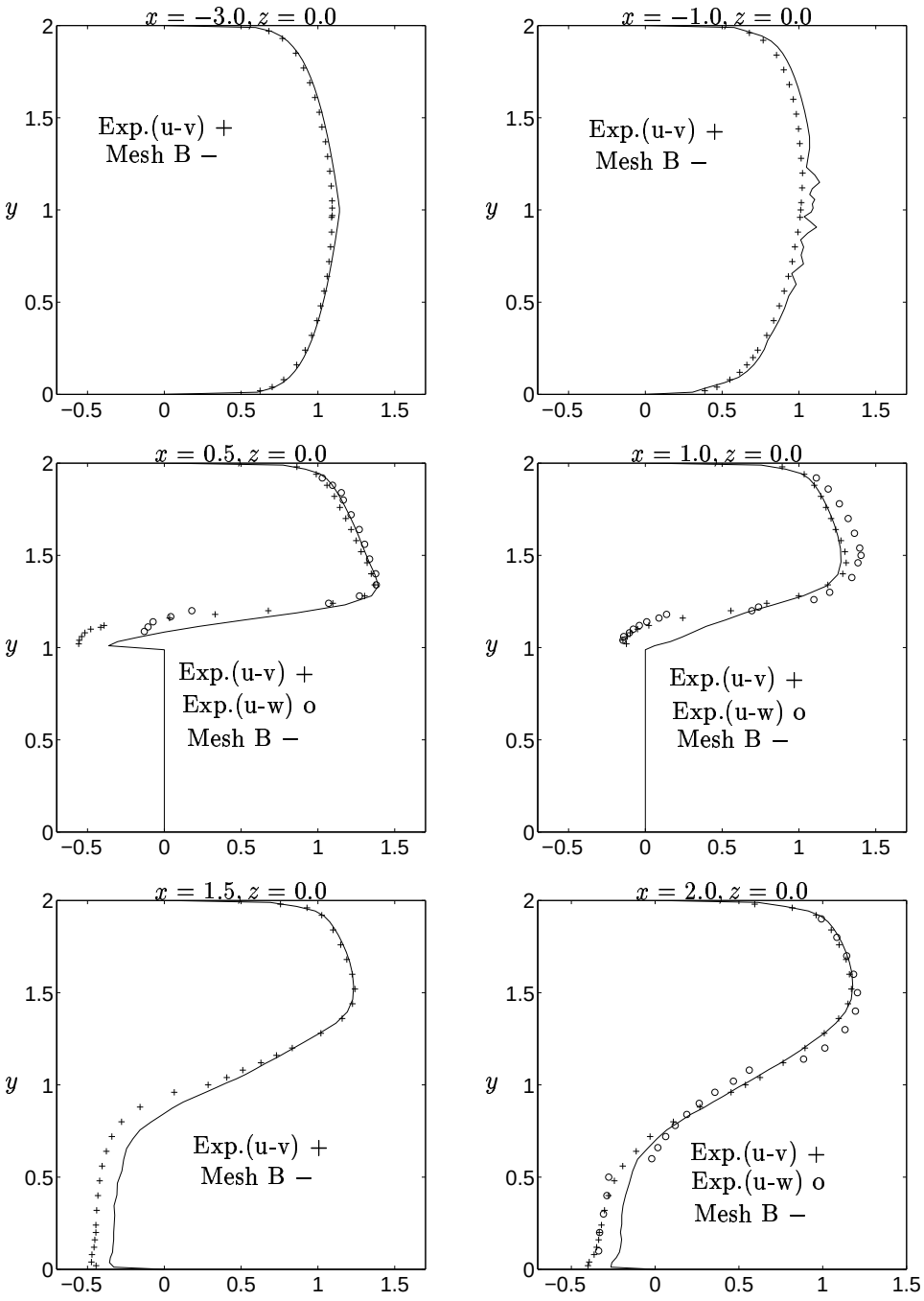

Figure 13: Mean velocity profile $\langle \bar{u} \rangle_t$. Mesh B.

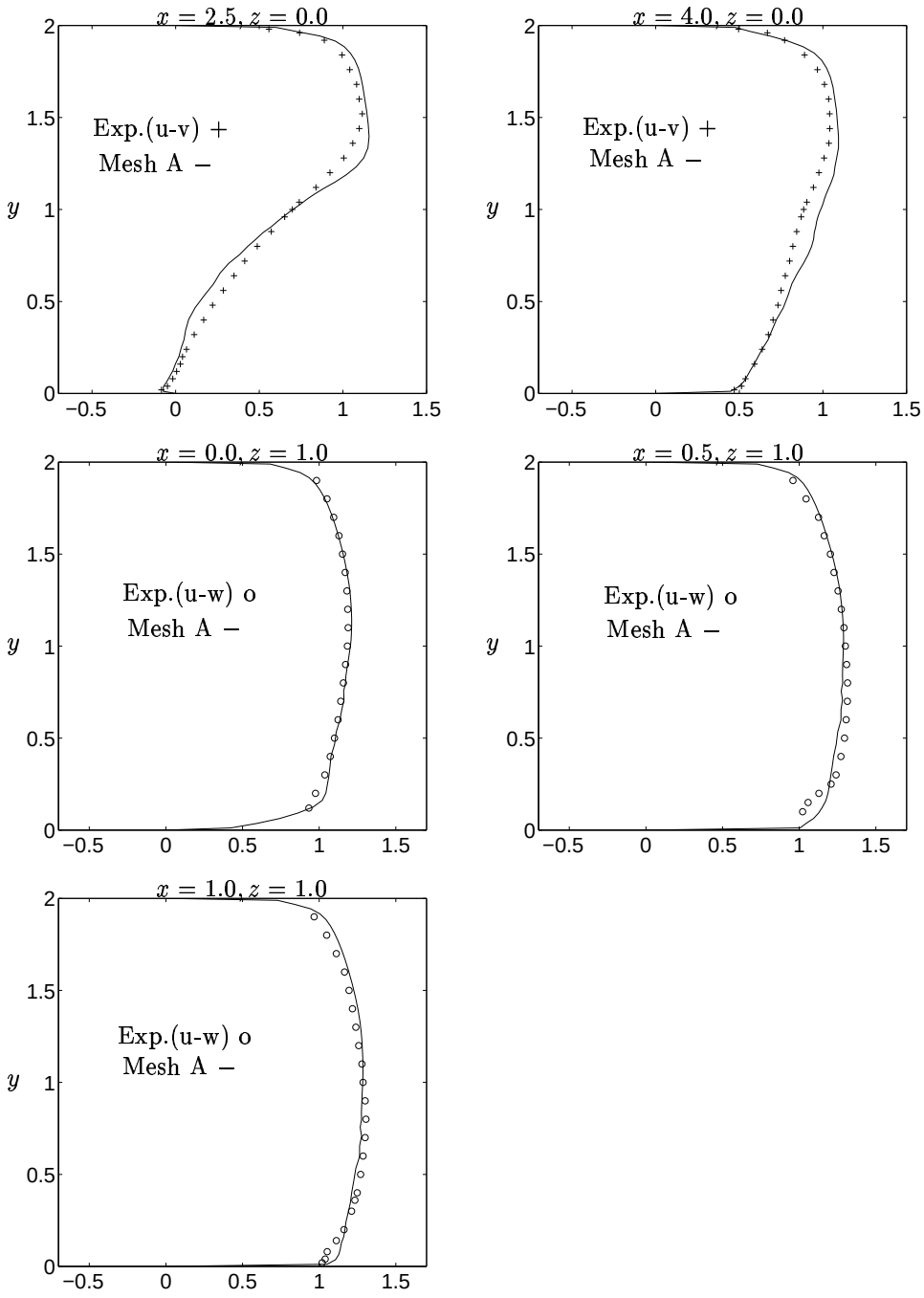

Figure 14: Mean velocity profile $\langle \bar{u} \rangle_t$. Mesh A.

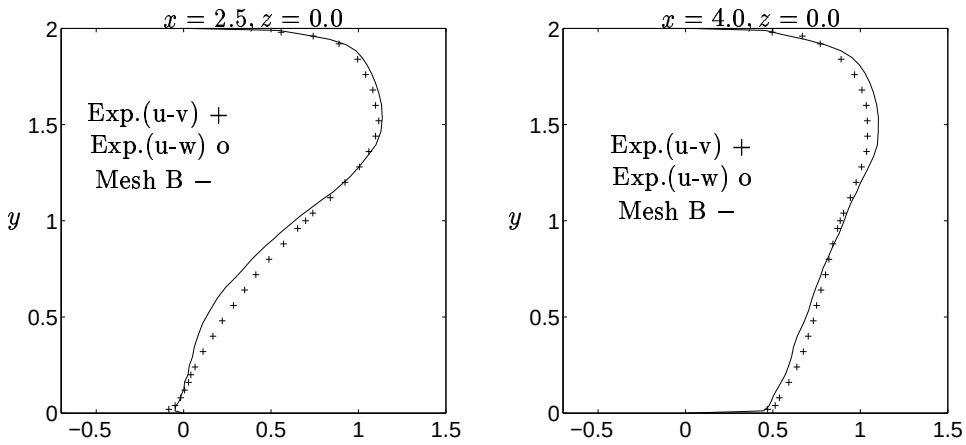

Figure 15: Mean velocity profile $\langle \bar{u} \rangle_t$. Mesh B.

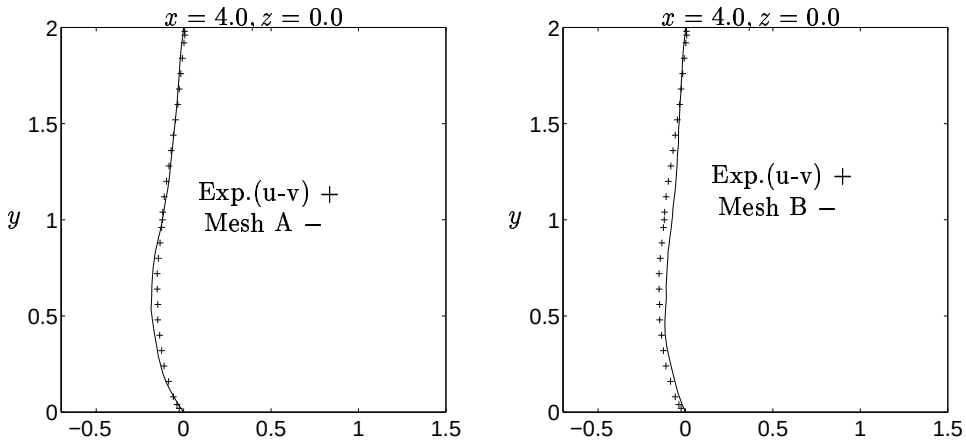

Figure 16: Mean velocity profile $\langle \bar{v} \rangle_t$. Mesh A and Mesh B.

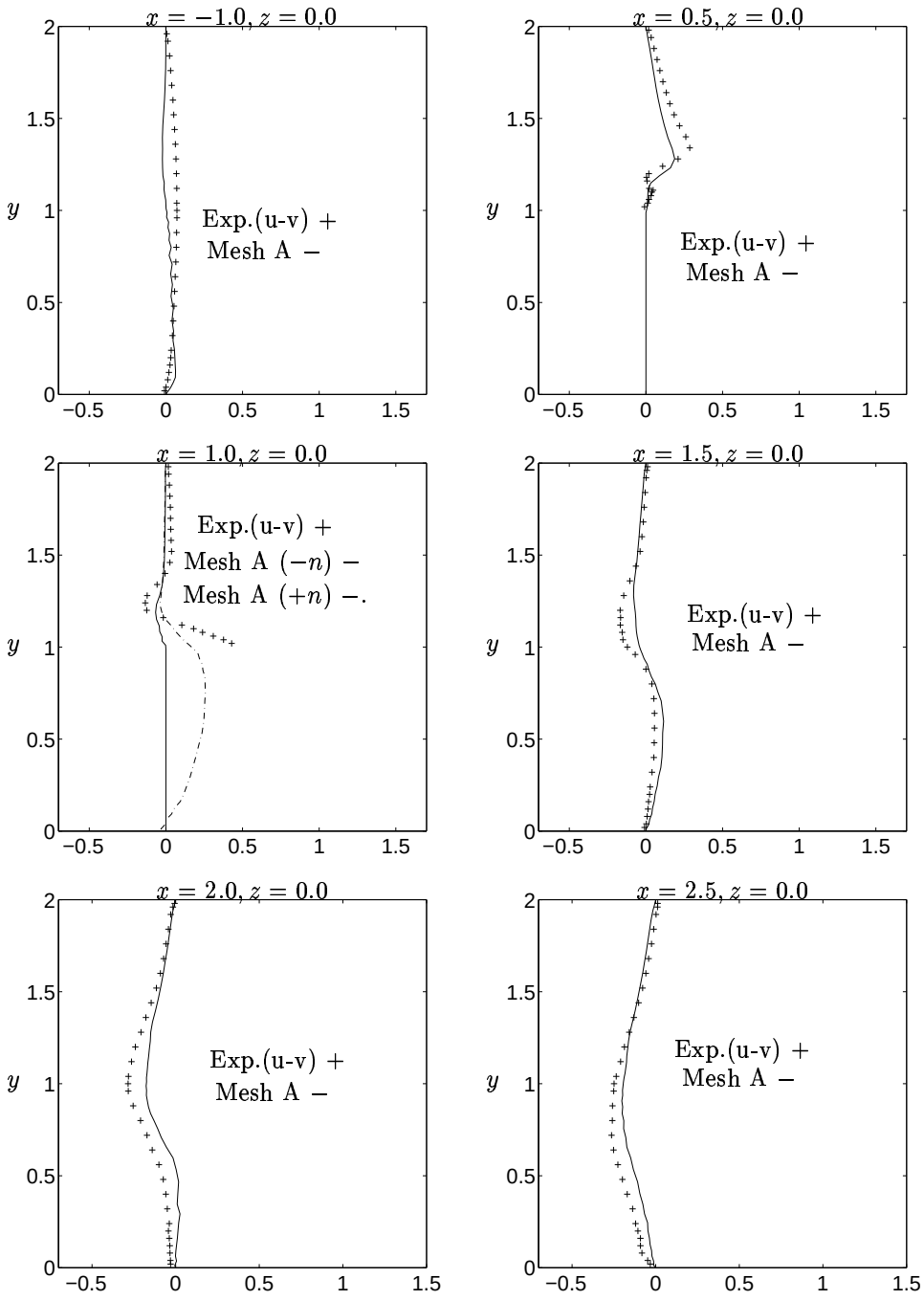

Figure 17: Mean velocity profile $\langle \bar{v} \rangle_t$. Mesh A. In the case $x = 1.0, z = 0.0$ is with $(-n)$ denoted one node before the surface and with $(+n)$ one node after the surface. (In the present work there is no nodes at the surface of the cube!)

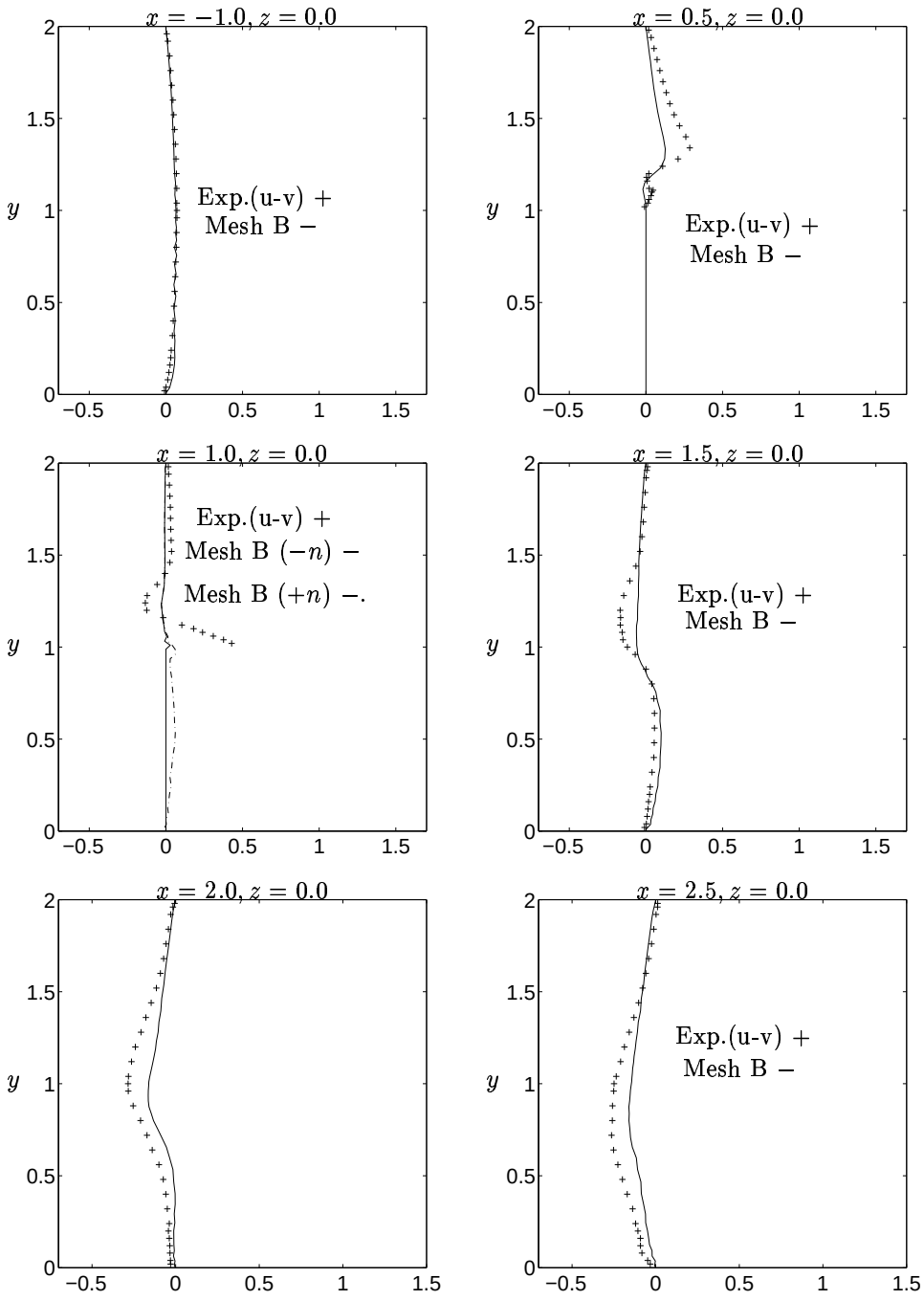

Figure 18: Mean velocity profile $\langle \bar{v} \rangle_t$. Mesh B. In the case $x = 1.0, z = 0.0$ is with $(-n)$ denoted one node before the surface and with $(+n)$ one node after the surface. (In the present work there is no nodes at the surface of the cube!)

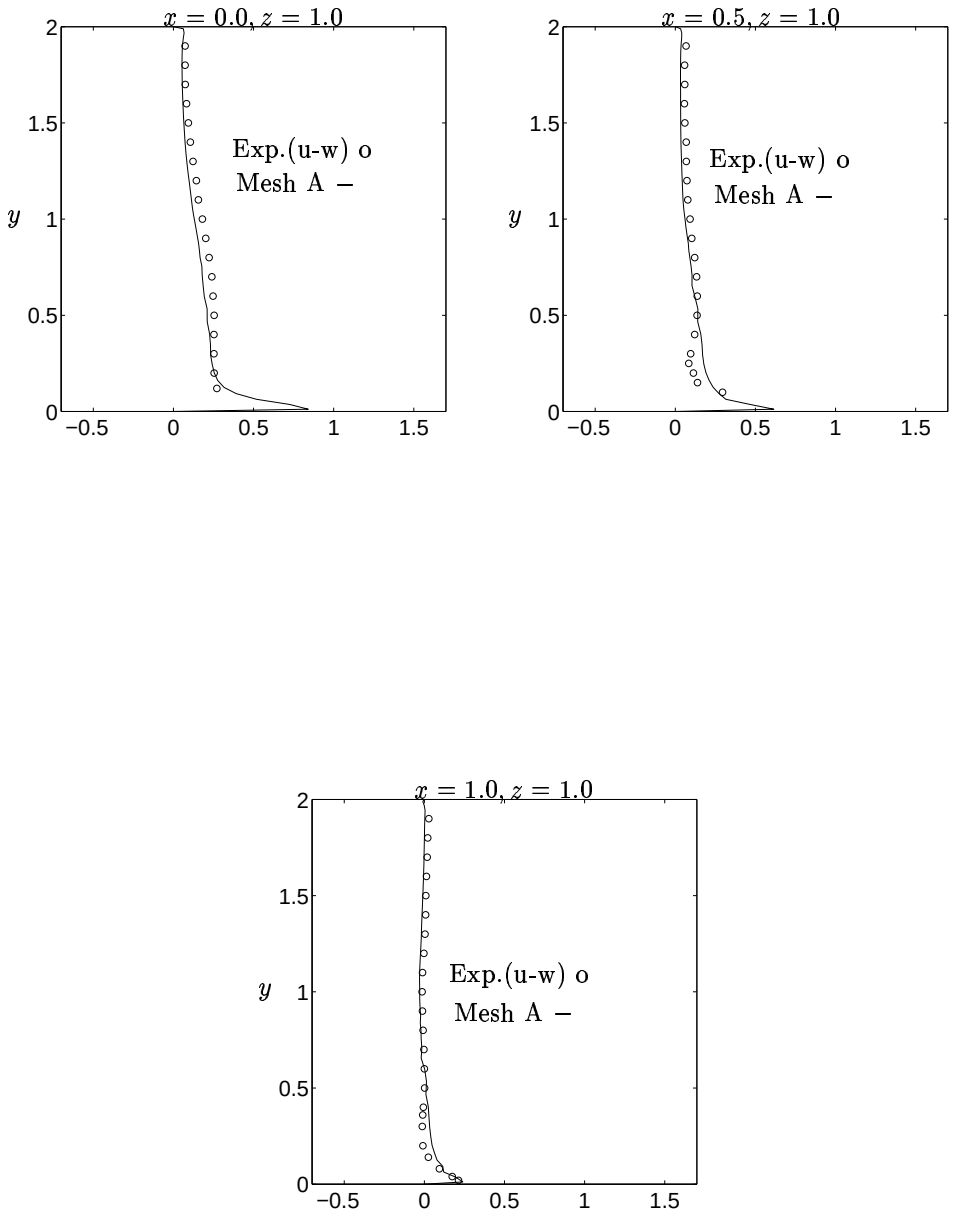

Figure 19: Mean velocity profile $\langle \bar{w} \rangle_t$. Mesh A.

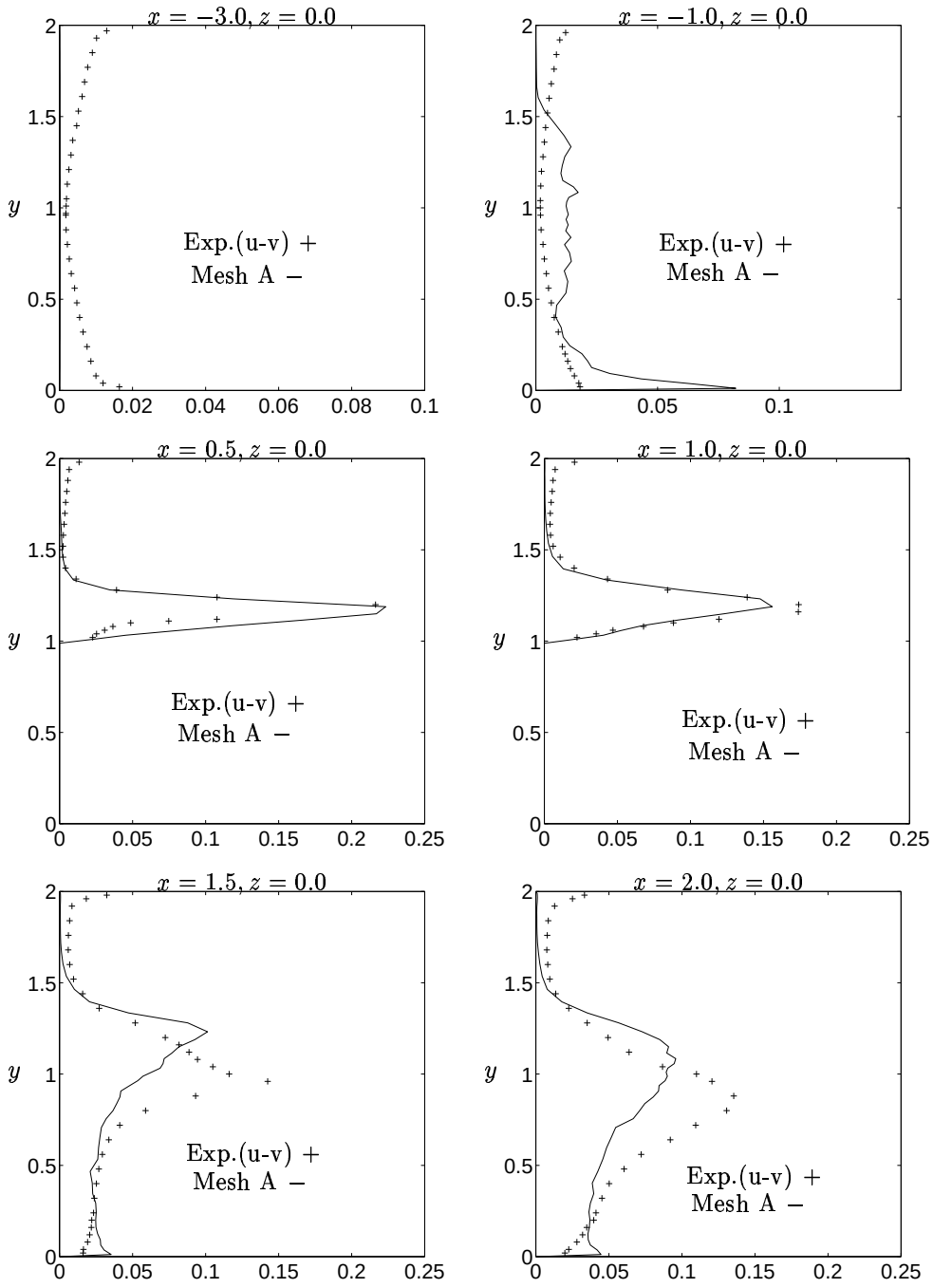

Figure 20: Mean turbulent stress $\langle \overline{u'^2} \rangle_t$. Mesh A.

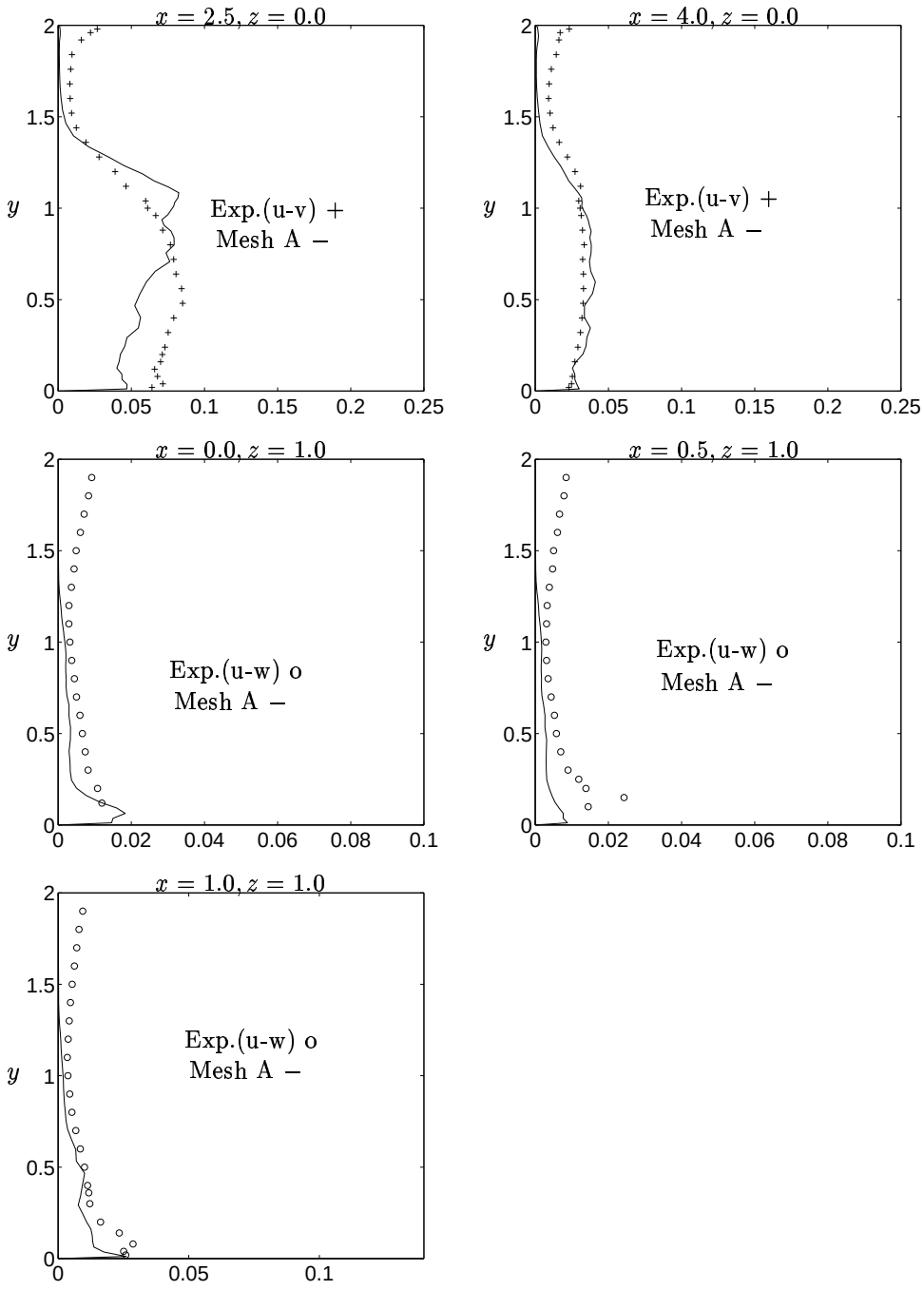

Figure 21: Mean turbulent stress $\langle \overline{u'^2} \rangle_t$. Mesh A.

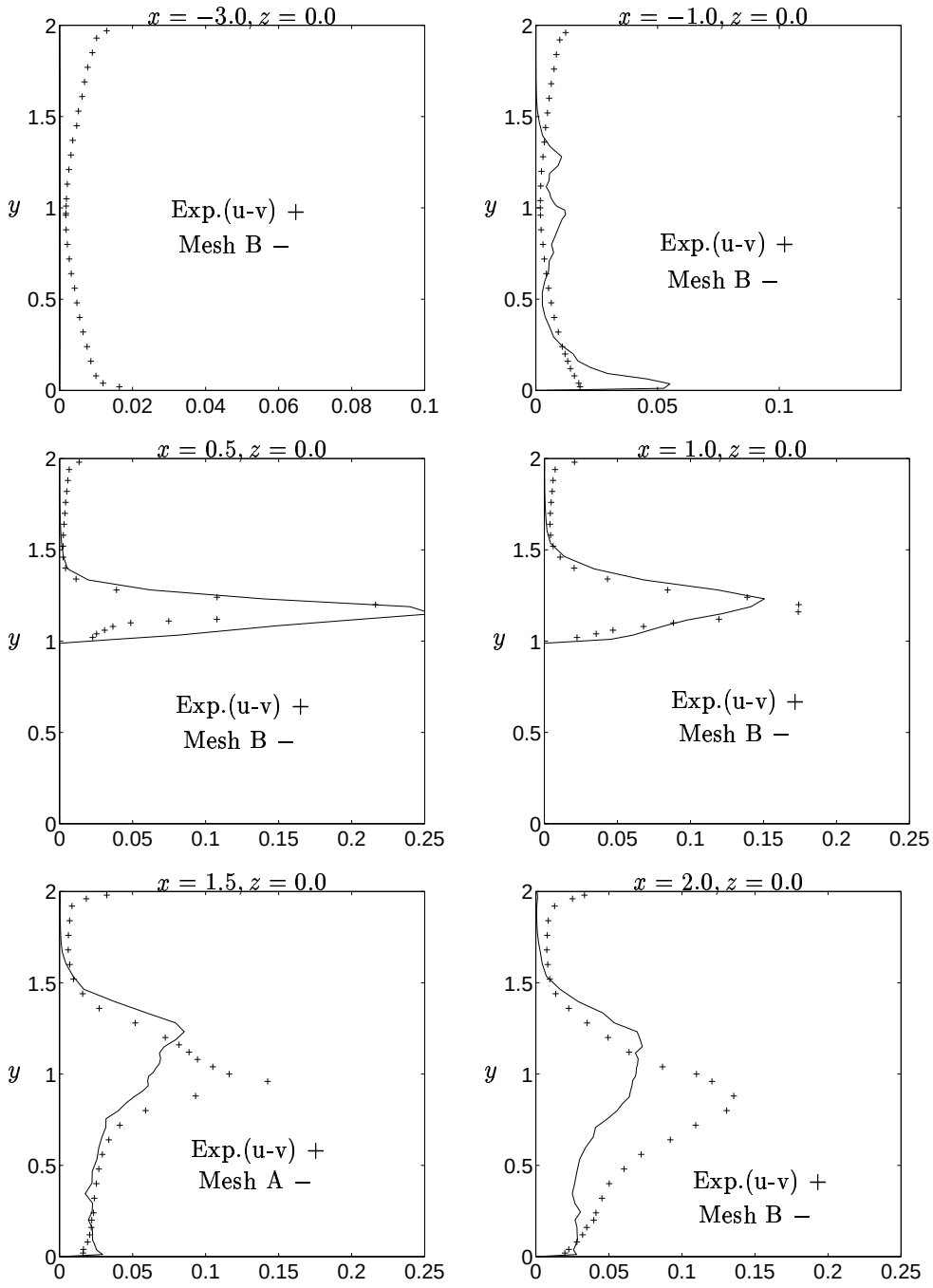

Figure 22: Mean turbulent stress $\langle \overline{u'^2} \rangle_t$. Mesh B.

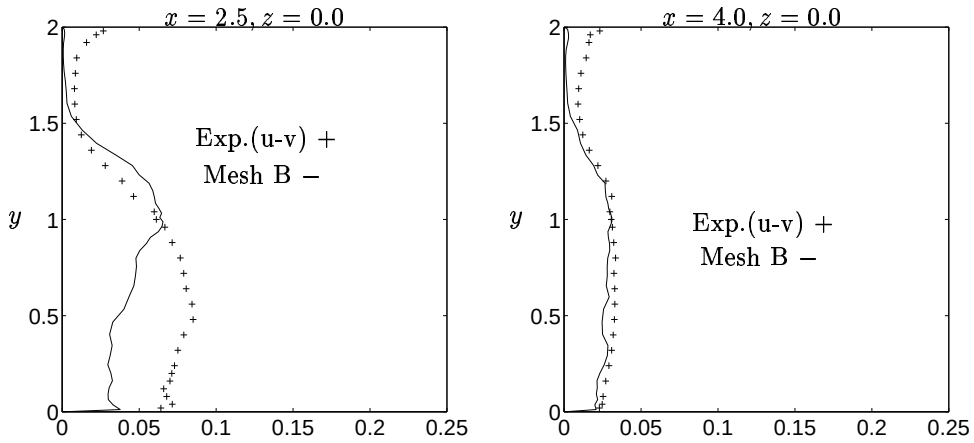

Figure 23: Mean turbulent stress $\langle \overline{u'^2} \rangle_t$. Mesh B.

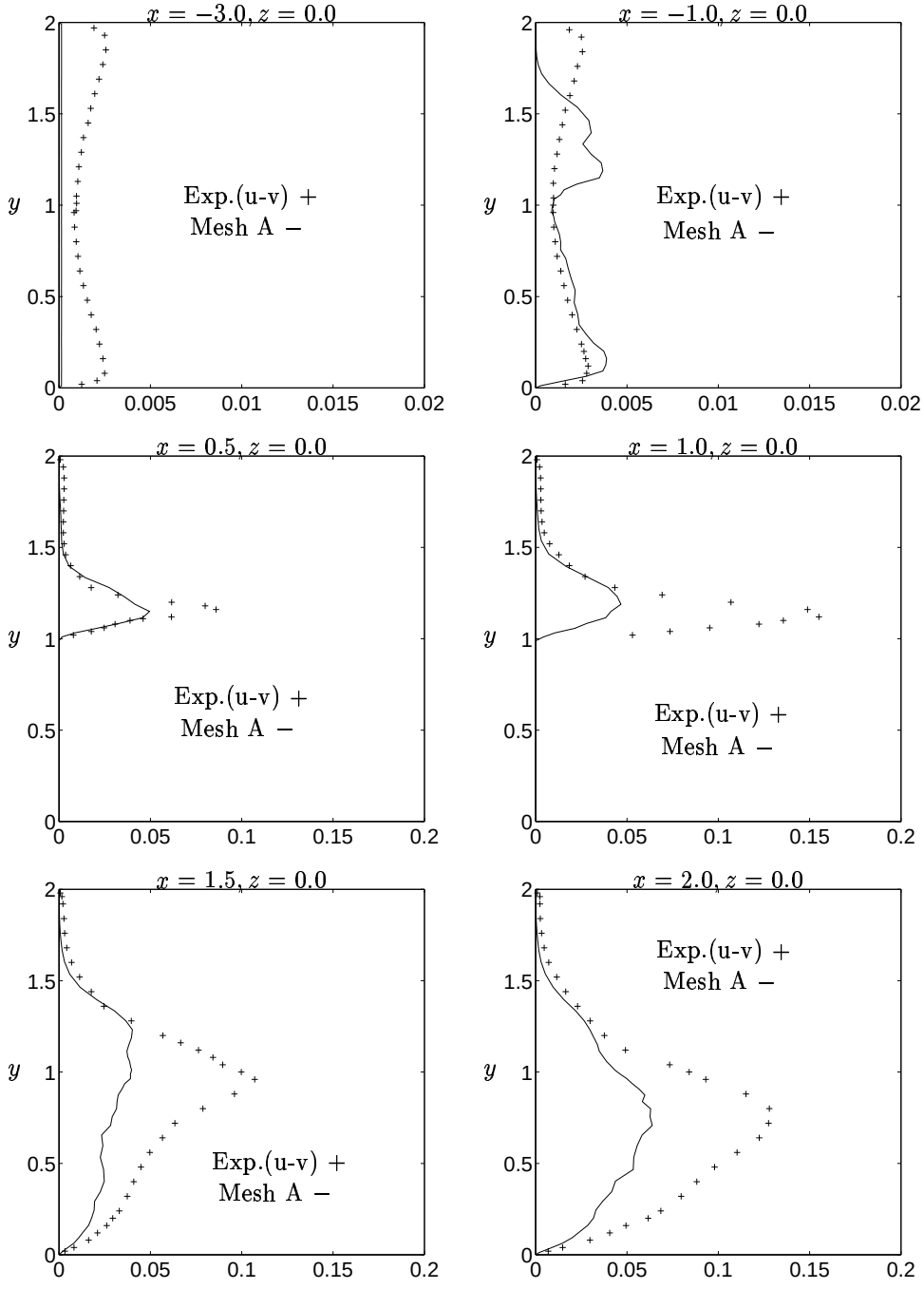

Figure 24: Mean turbulent stress $\langle \overline{v'^2} \rangle_t$. Mesh A.

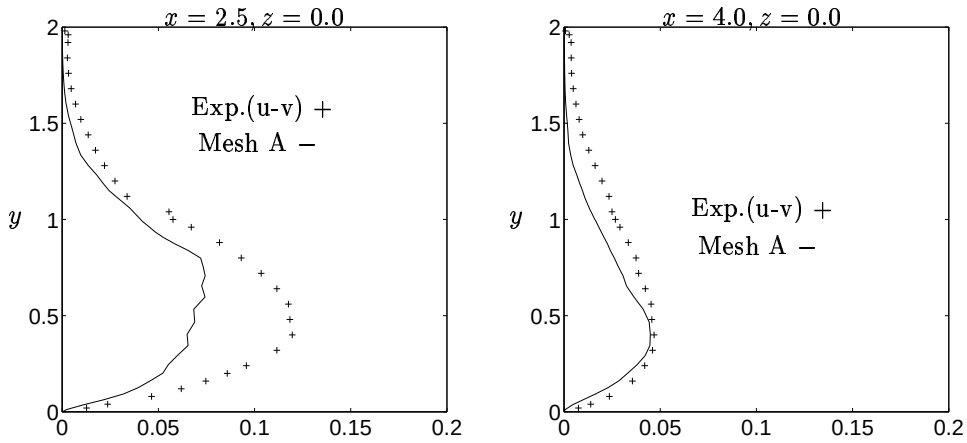

Figure 25: Mean turbulent stress $\langle \overline{v'^2} \rangle_t$. Mesh A.

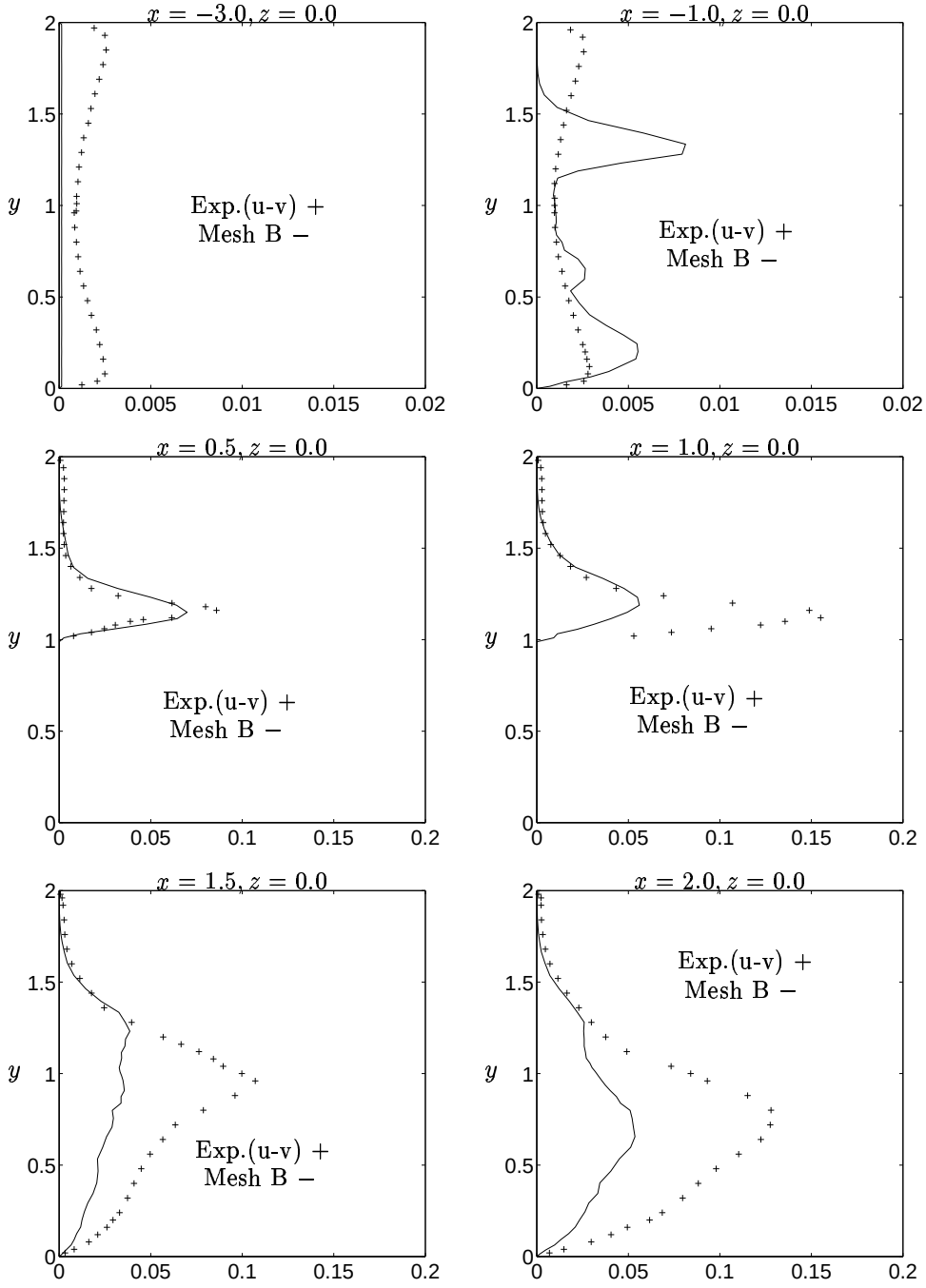

Figure 26: Mean turbulent stress $\langle \overline{v'^2} \rangle_t$. Mesh B.

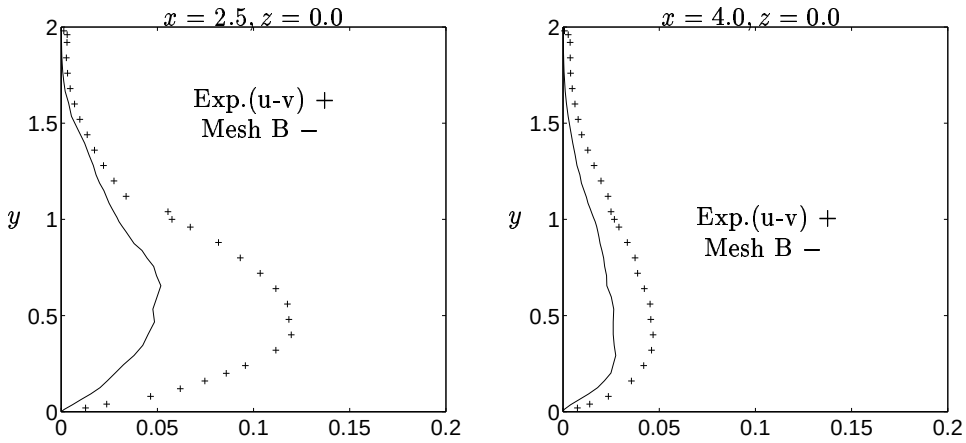

Figure 27: Mean turbulent stress $\langle \overline{v'^2} \rangle_t$. Mesh B.

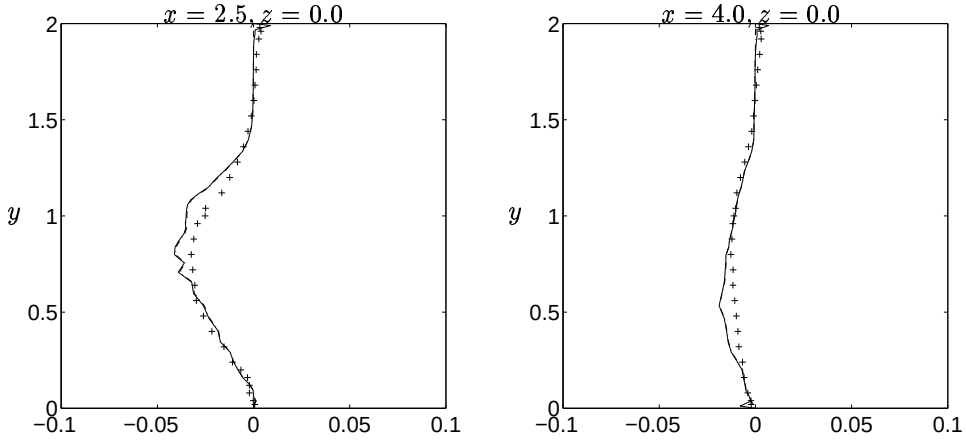

Figure 28: Mean turbulent stresses $\langle \overline{u'v'} \rangle_t$ $'-.'$ and $\langle \overline{u'v'} \rangle_t + \langle \tau_{12} \rangle_t$ $'-'$. Mesh A.

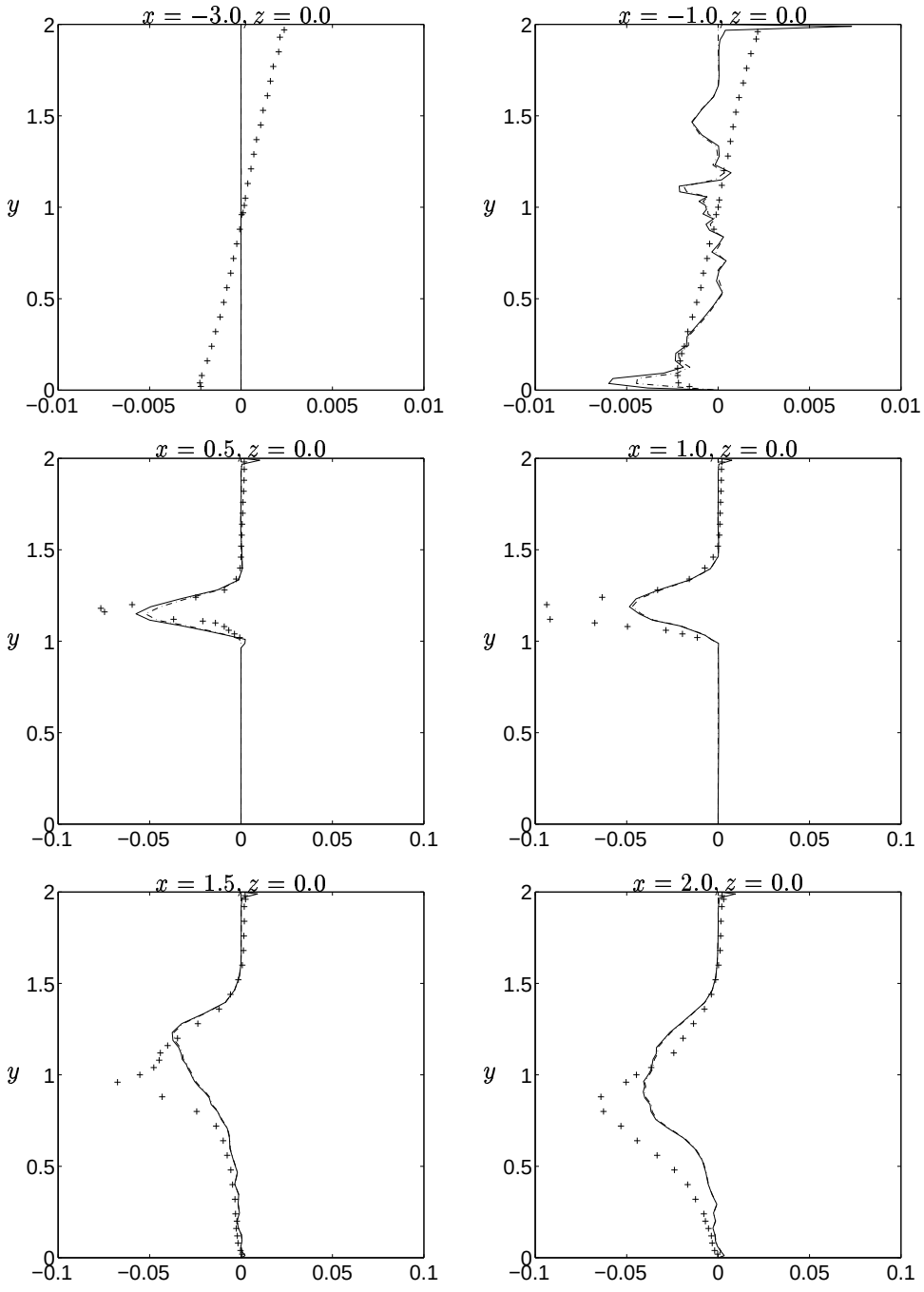

Figure 29: Comparation between resolved mean turbulent stresses $\langle\overline{u'v'}\rangle_t$ $'-.'$ and $\langle\overline{u'v'}\rangle_t + \langle\tau_{12}\rangle_t$ $'-'$. Exp. $(u-v)$ is denoted with $+$. Mesh A.

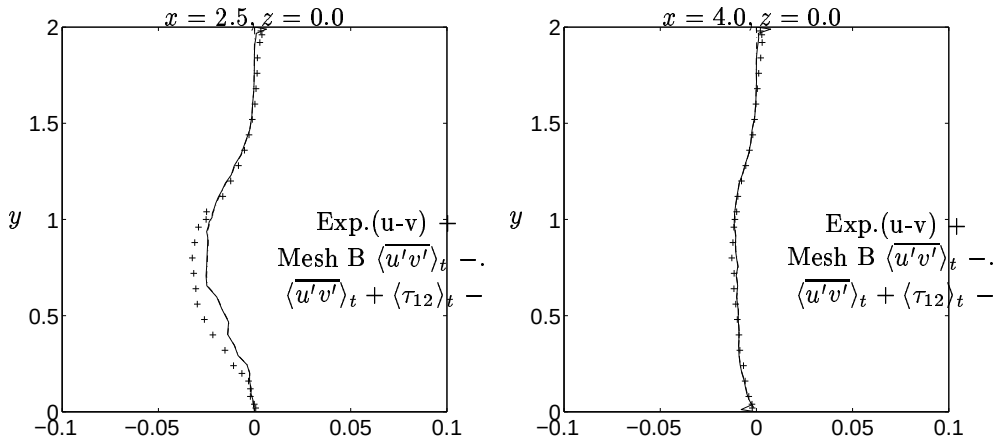

Figure 30: Mean turbulent stresses $\langle\overline{u'v'}\rangle_t$and $\overline{u'v'} + \langle\tau_{12}\rangle_t$. Mesh B.

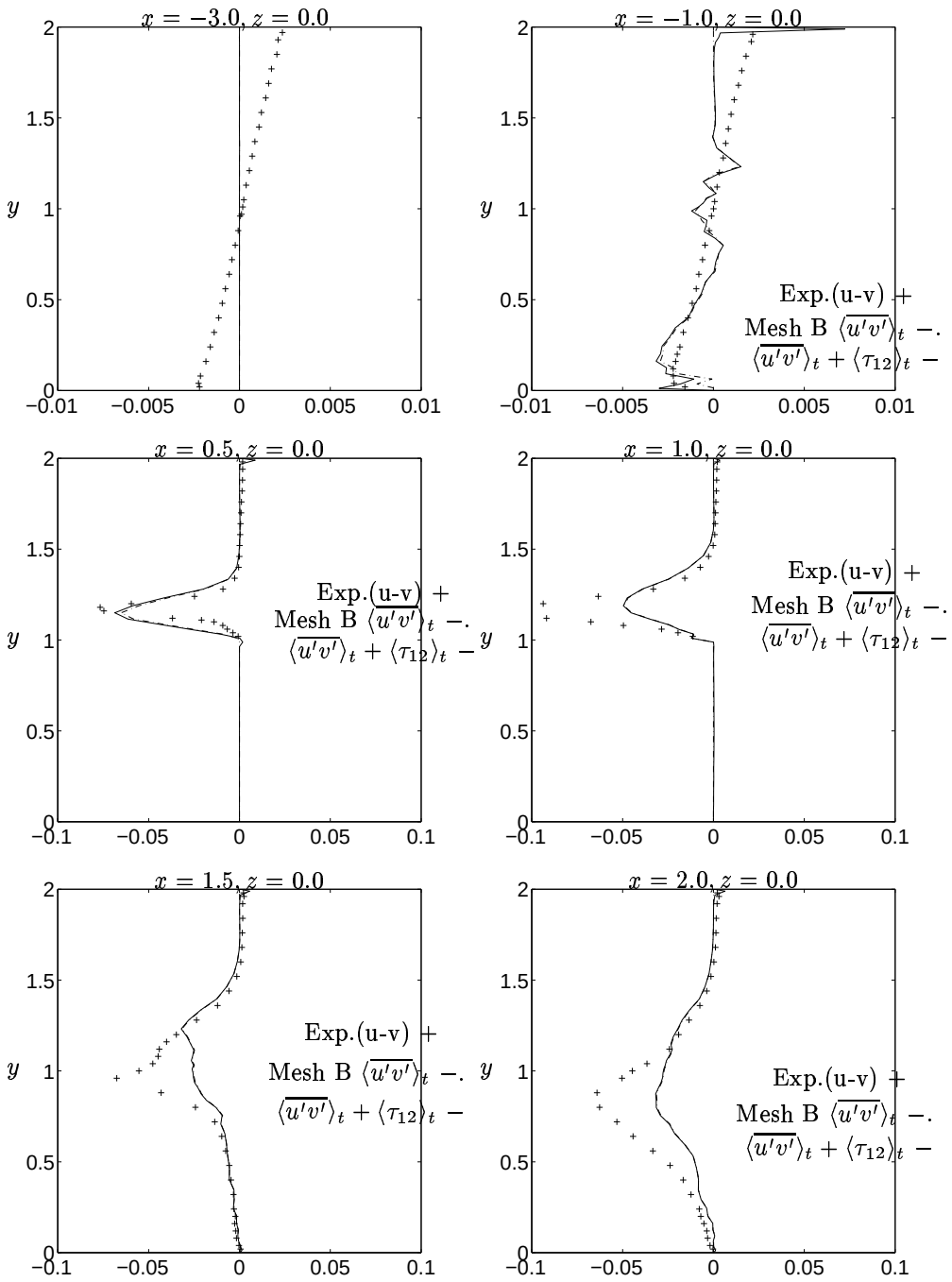

Figure 31: Comparation between resolved mean turbulent stresses $\langle\overline{u'v'}\rangle_t$ and $\langle\overline{u'v'}\rangle_t + \langle\tau_{12}\rangle_t$. Mesh B.

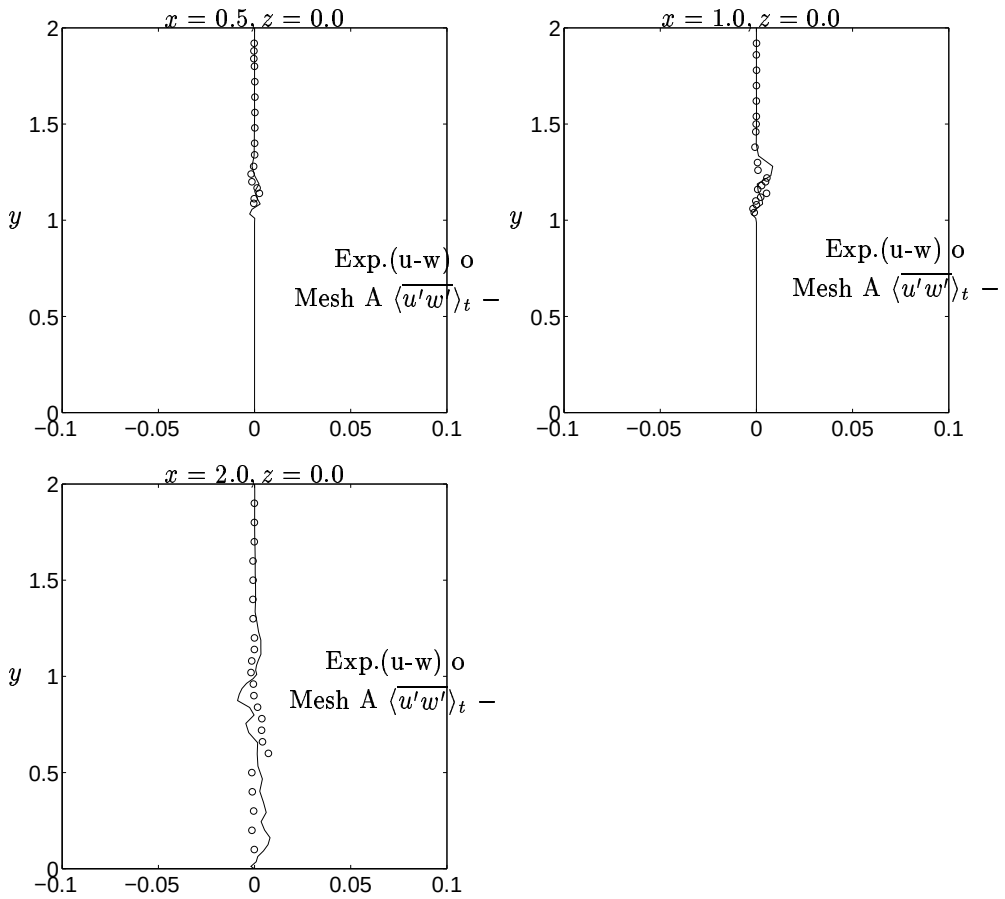

Figure 32: Mean turbulent stress $\langle\overline{u'w'}\rangle_t$. Mesh A.

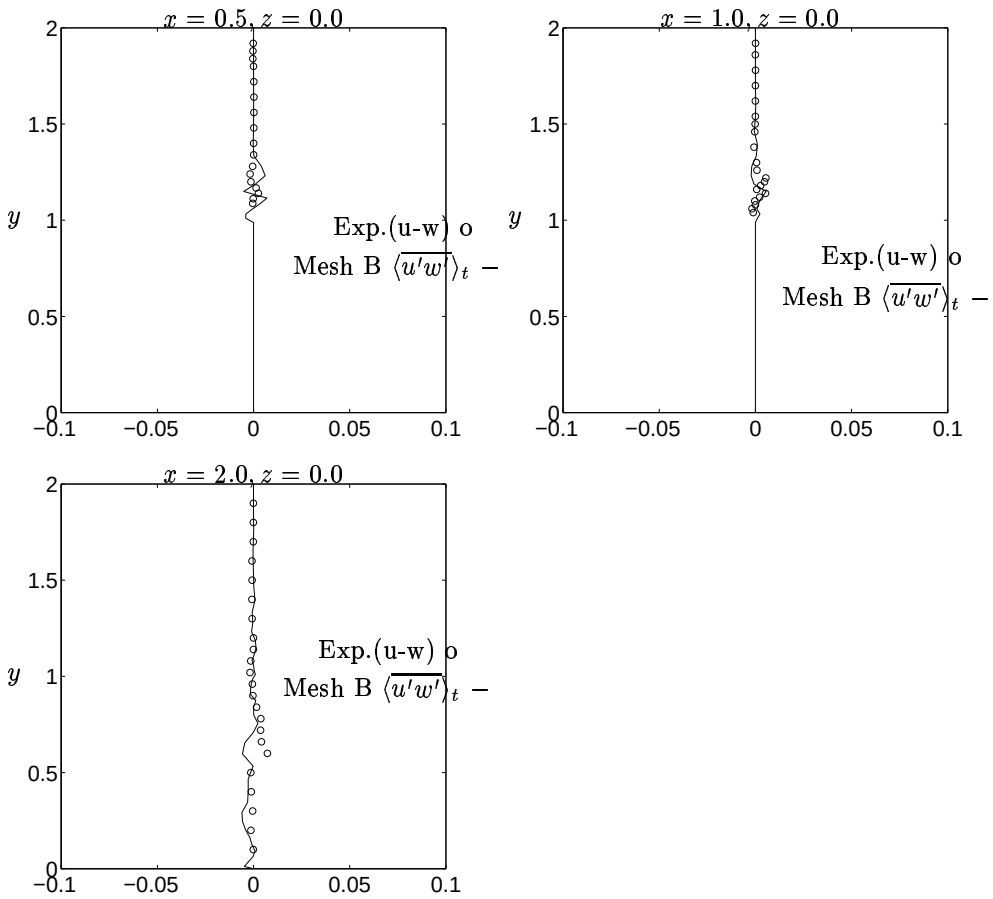

Figure 33: Mean turbulent stress $\langle\overline{u'w'}\rangle_t$. Mesh B.

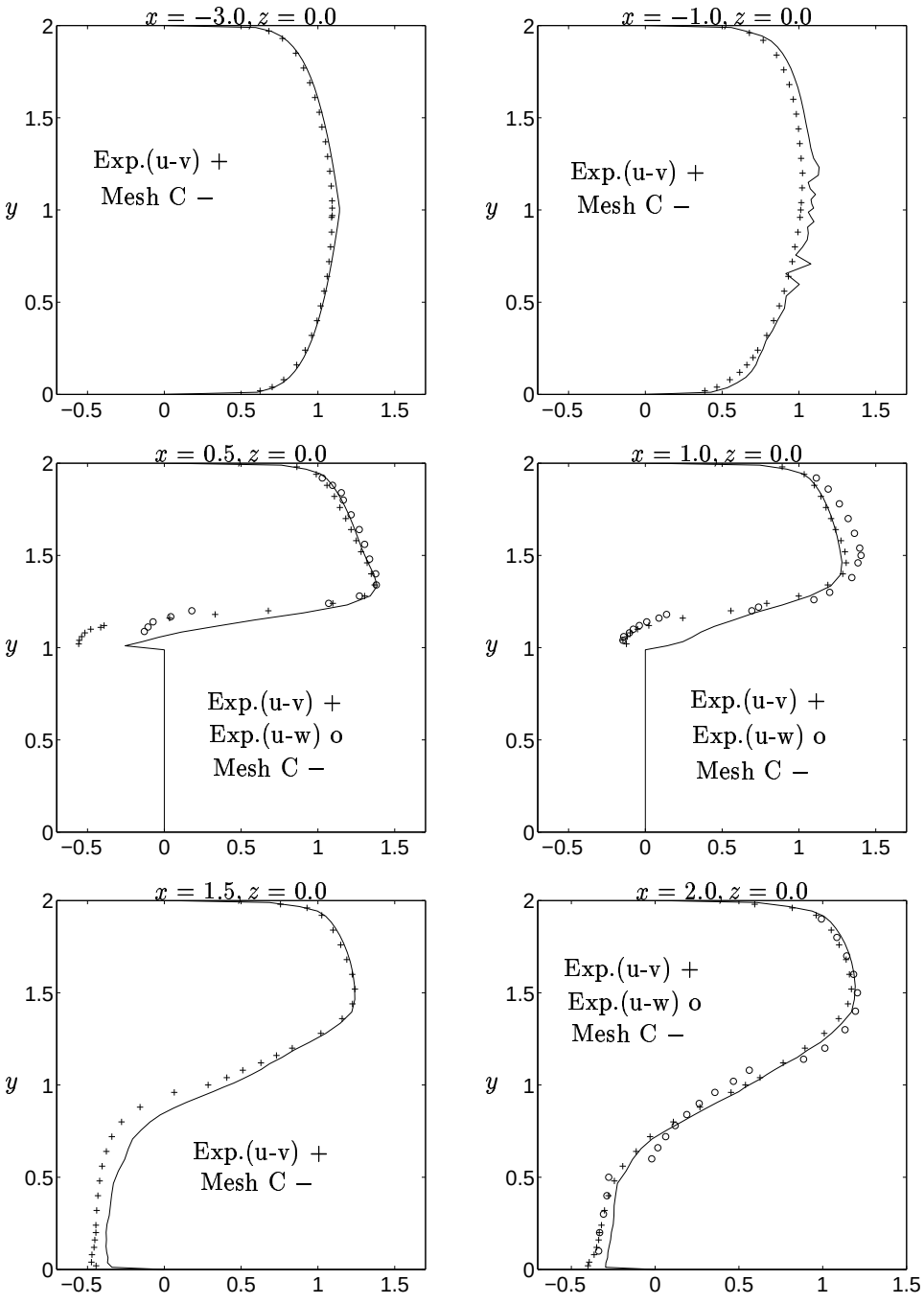

Figure 34: Mean velocity profile $\langle \bar{u} \rangle_t$. Mesh C.

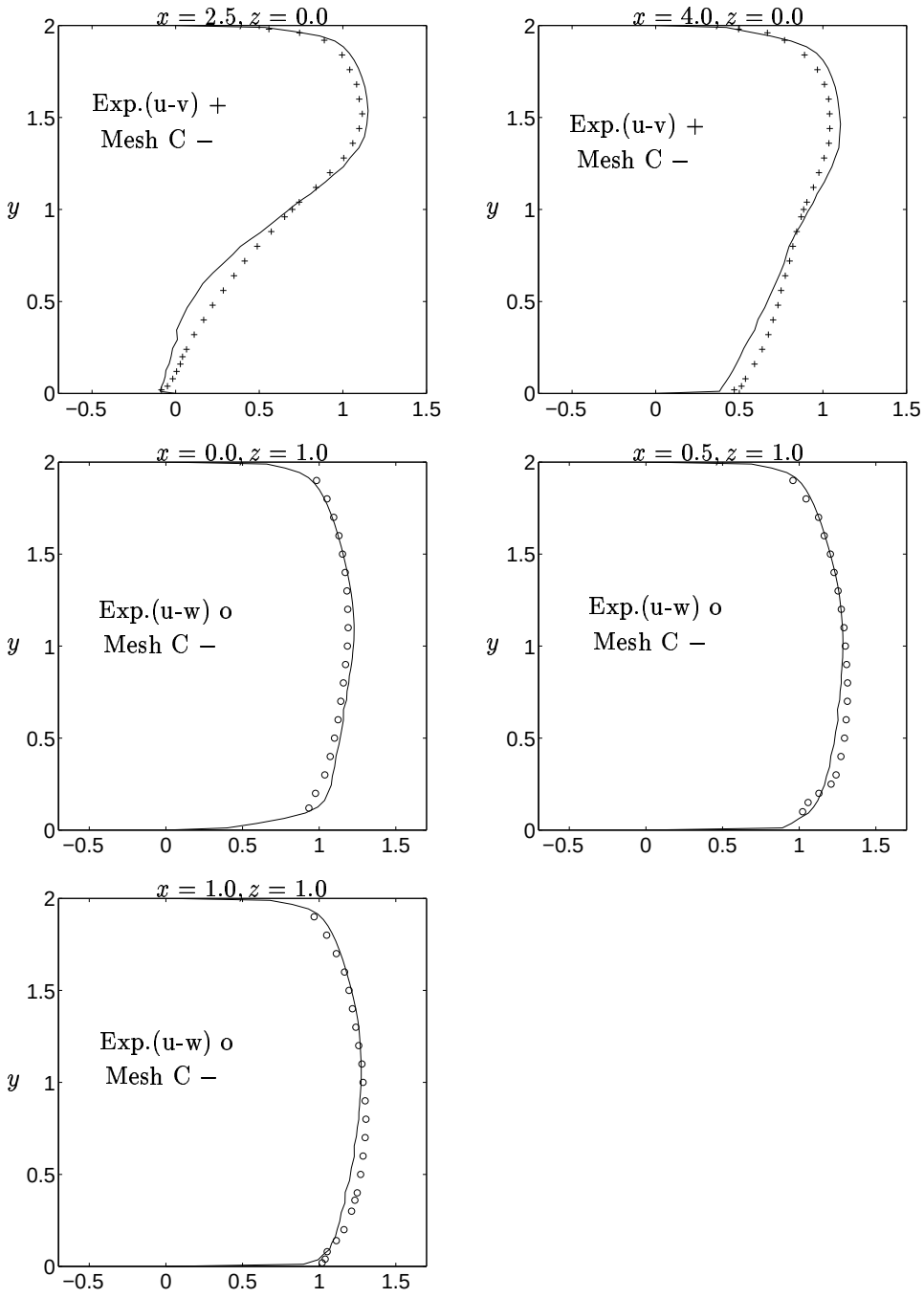

Figure 35: Mean velocity profile $\langle \bar{u} \rangle_t$. Mesh C.

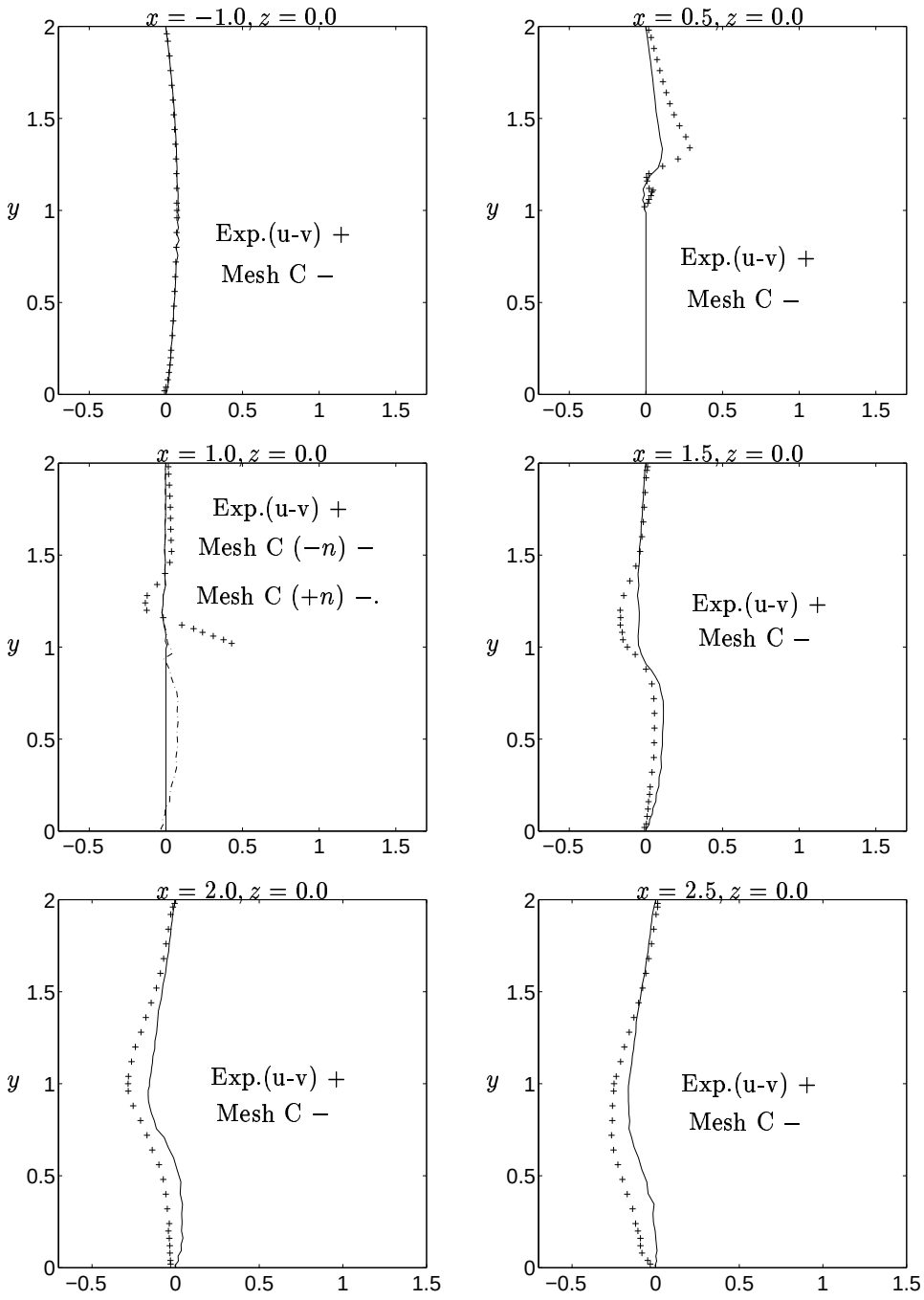

Figure 36: Mean velocity profile $\langle \bar{v} \rangle_t$. Mesh C. In the case $x = 1.0, z = 0.0$ is with $(-n)$ denoted one node before the surface and with $(+n)$ one node after the surface. (In the present work there is no nodes at the surface of the cube!)

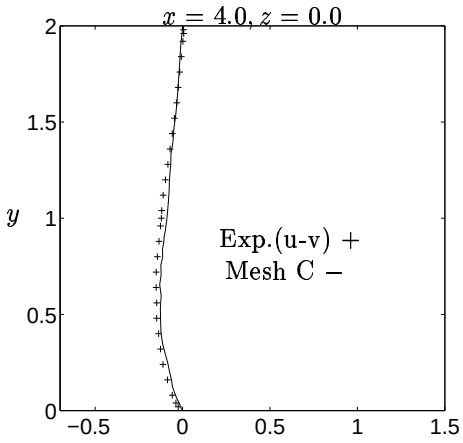

Figure 37: Mean velocity profile $\langle \bar{v} \rangle_t$. Mesh C.

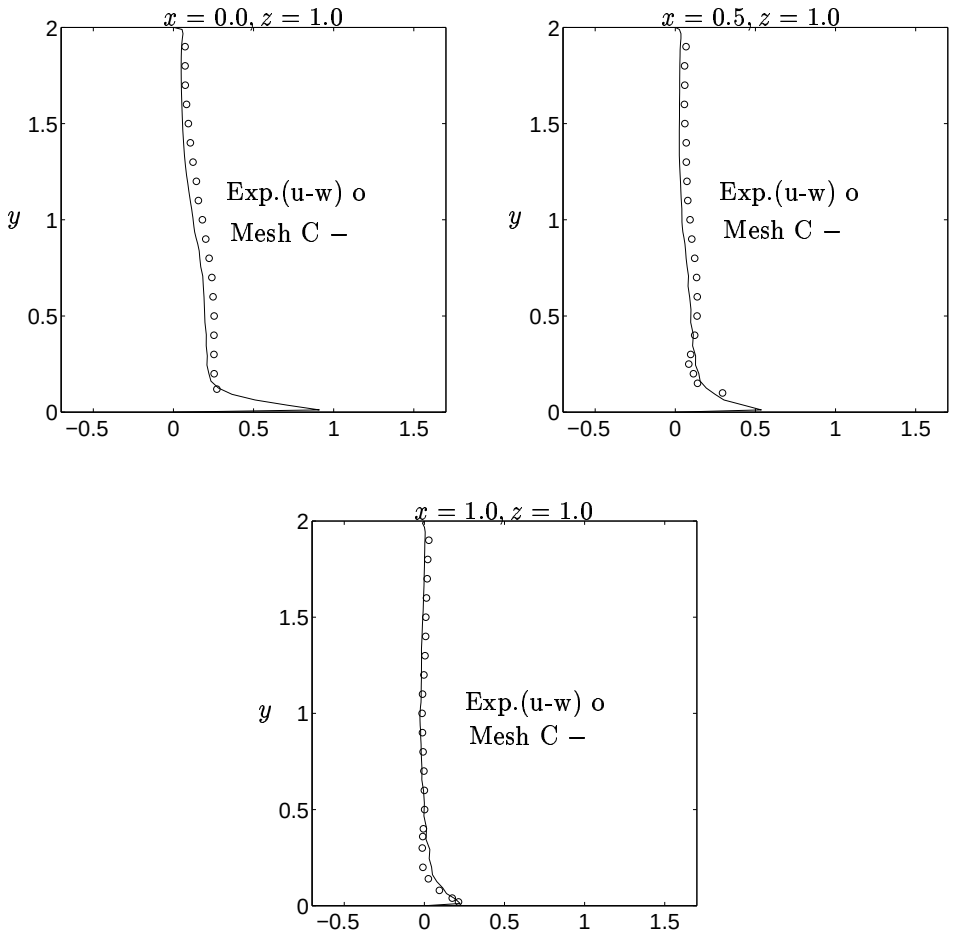

Figure 38: Mean velocity profile $\langle \bar{w} \rangle_t$. Mesh C.

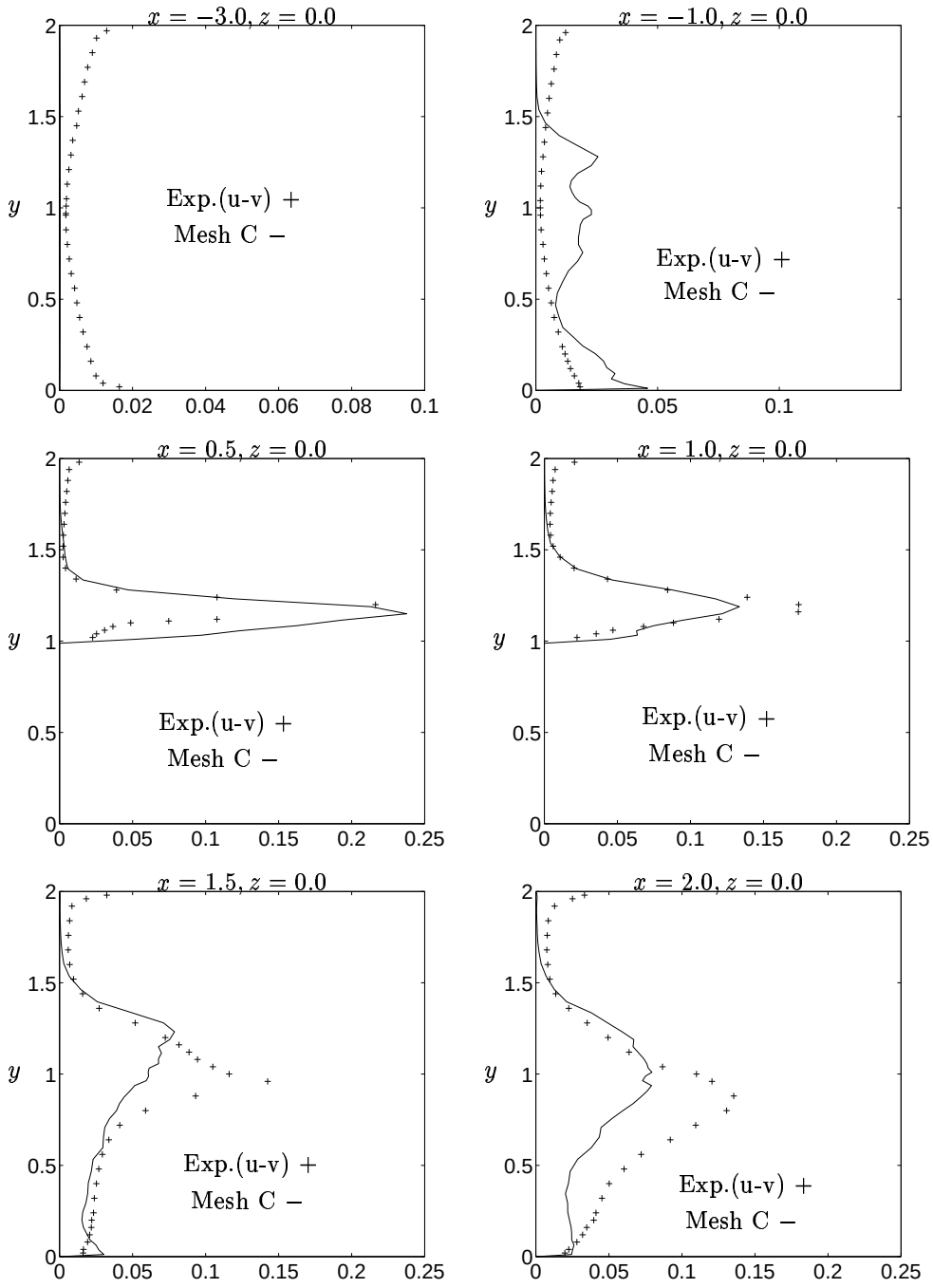

Figure 39: Mean turbulent stress $\langle \overline{u'^2} \rangle_t$. Mesh C.

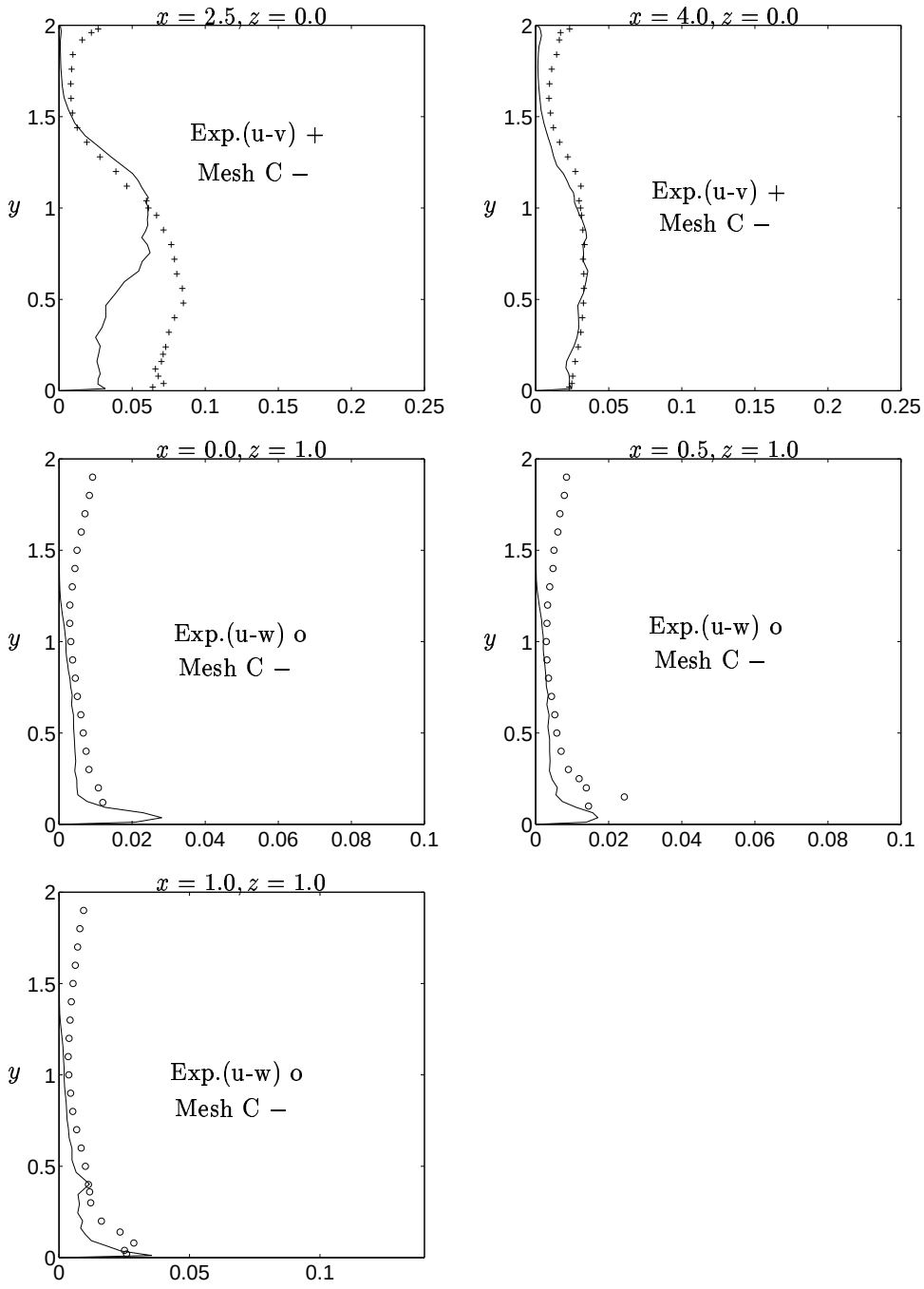

Figure 40: Mean turbulent stress $\langle \overline{u'^2} \rangle_t$. Mesh C.

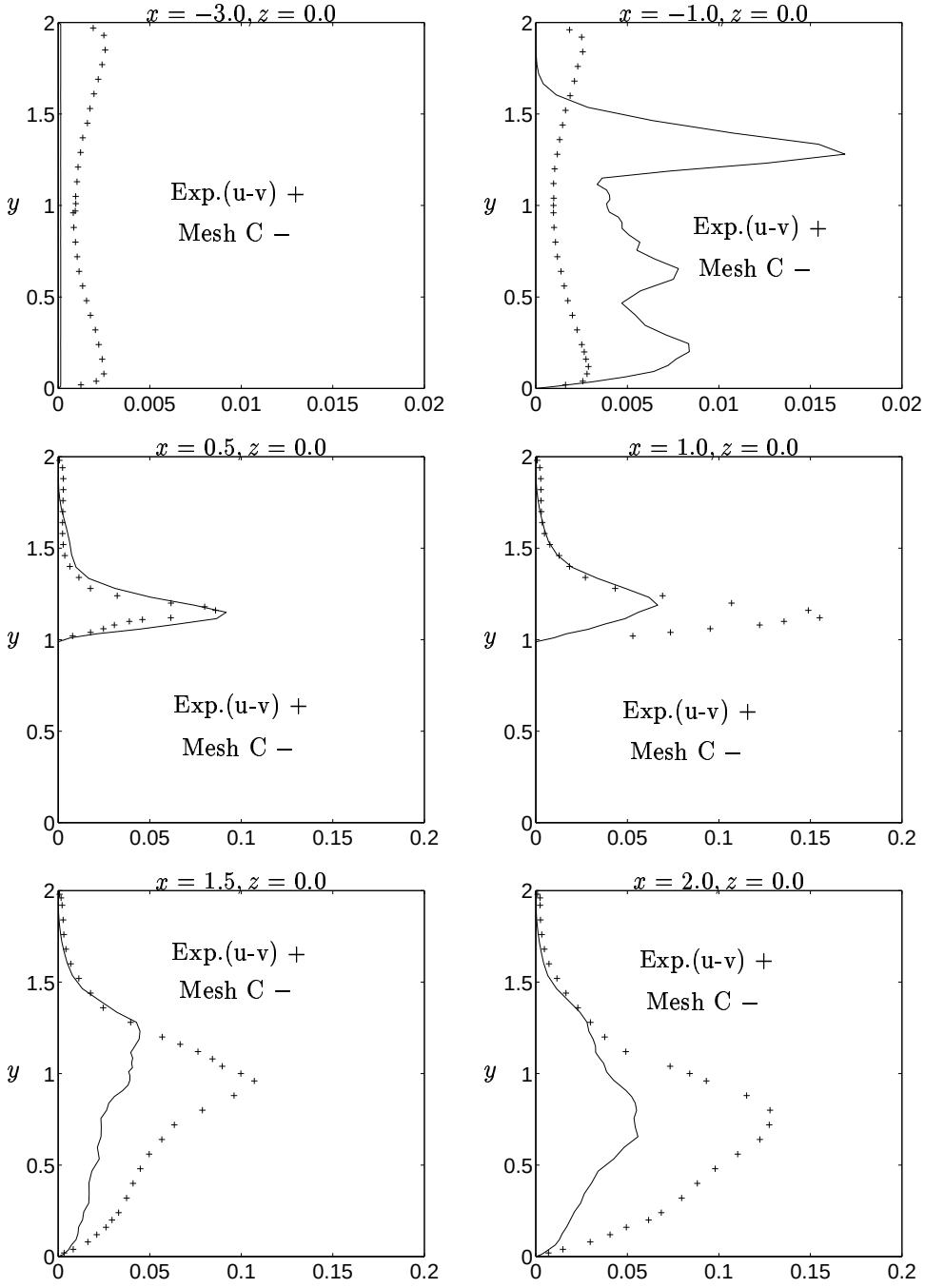

Figure 41: Mean turbulent stress $\langle \overline{v'^2} \rangle_t$. Mesh C.

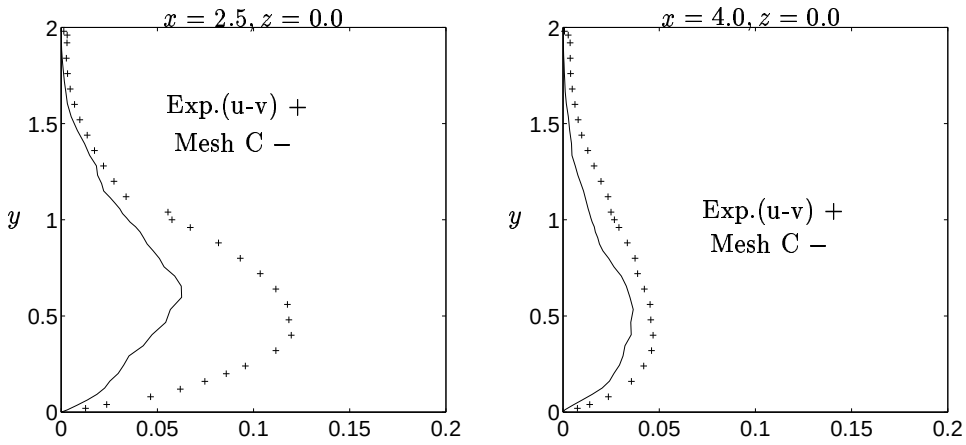

Figure 42: Mean turbulent stress $\langle \overline{v'^2} \rangle_t$. Mesh C.

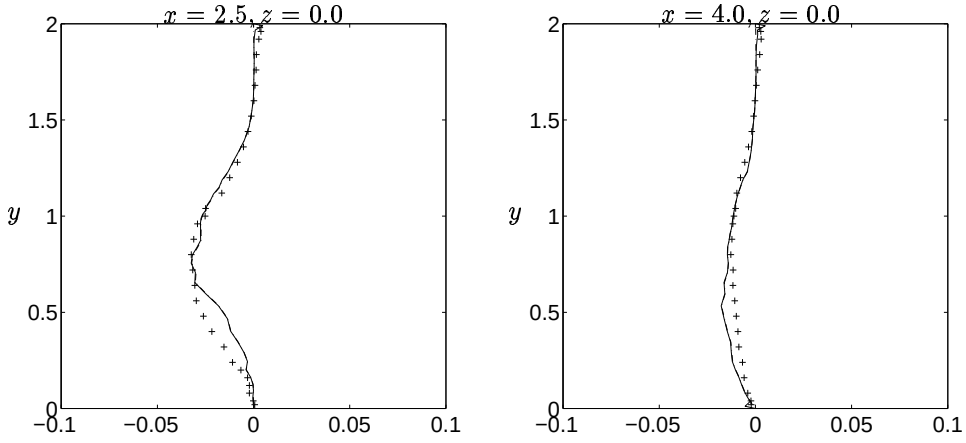

Figure 43: Comparation between resolved mean turbulent stresses $\langle \overline{u'v'} \rangle_t$ $'-.'$ and $\langle \overline{u'v'} \rangle_t + \langle \tau_{12} \rangle_t$ $'-'$. Exp. $(u - v)$ is denoted with $+$. Mesh C.

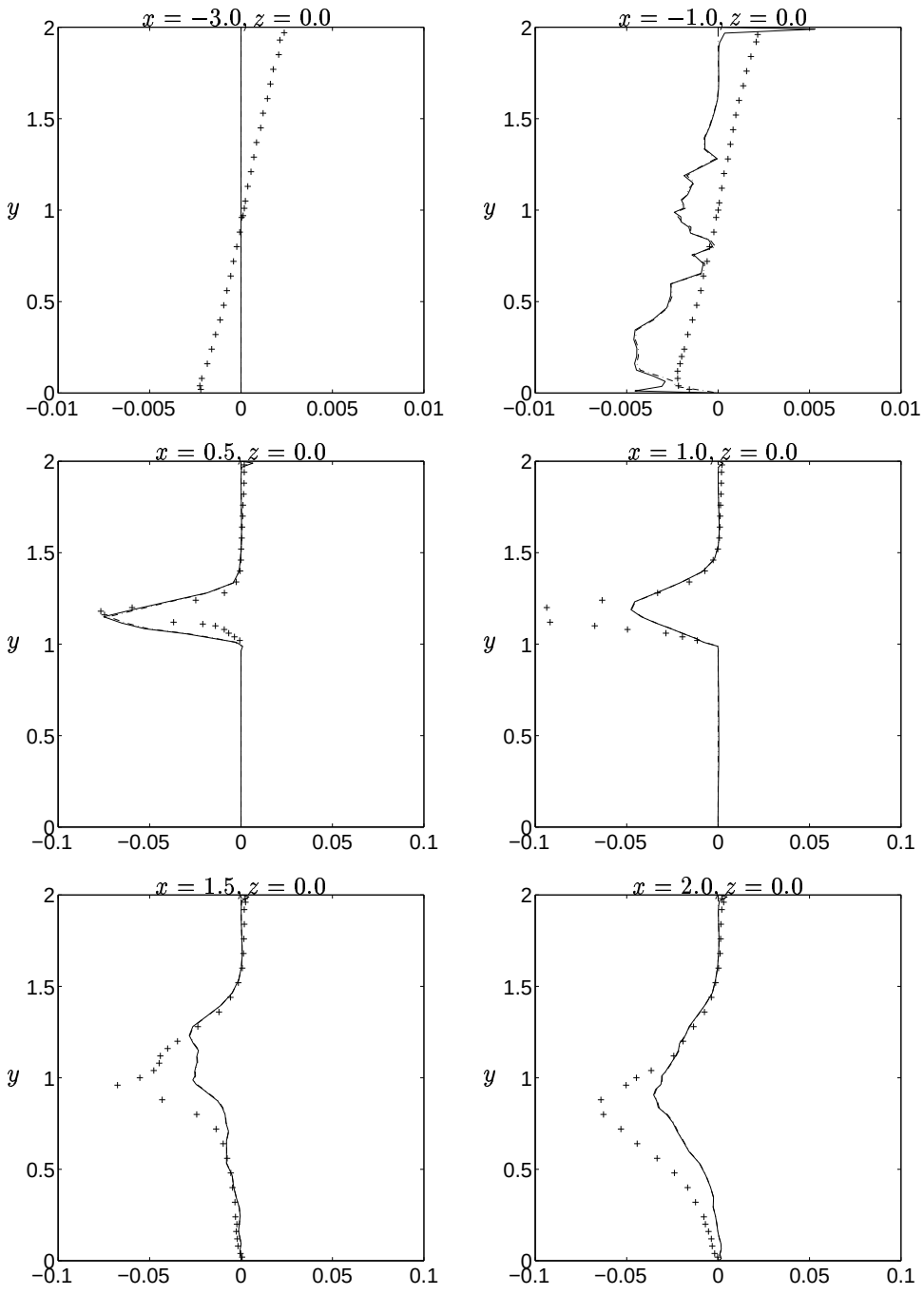

Figure 44: Comparation between resolved mean turbulent stresses $\langle \overline{u'v'} \rangle_t$ $'-.'$ and $\langle \overline{u'v'} \rangle_t + \langle \tau_{12} \rangle_t$ $'-'$. Exp. $(u - v)$ is denoted with $+$. Mesh C.

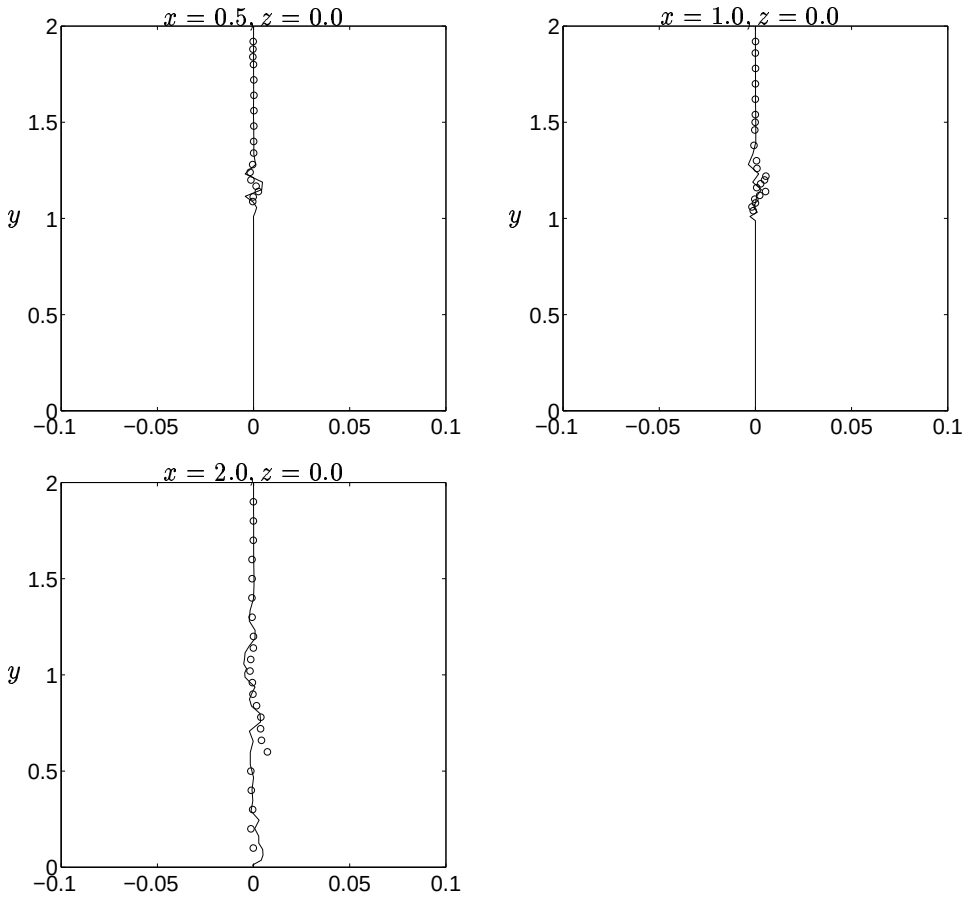

Figure 45: Mean turbulent stress $\langle \overline{u'w'} \rangle_t$ '-'. Exp.$(u - w)$ is denoted with 'o'. Mesh C.

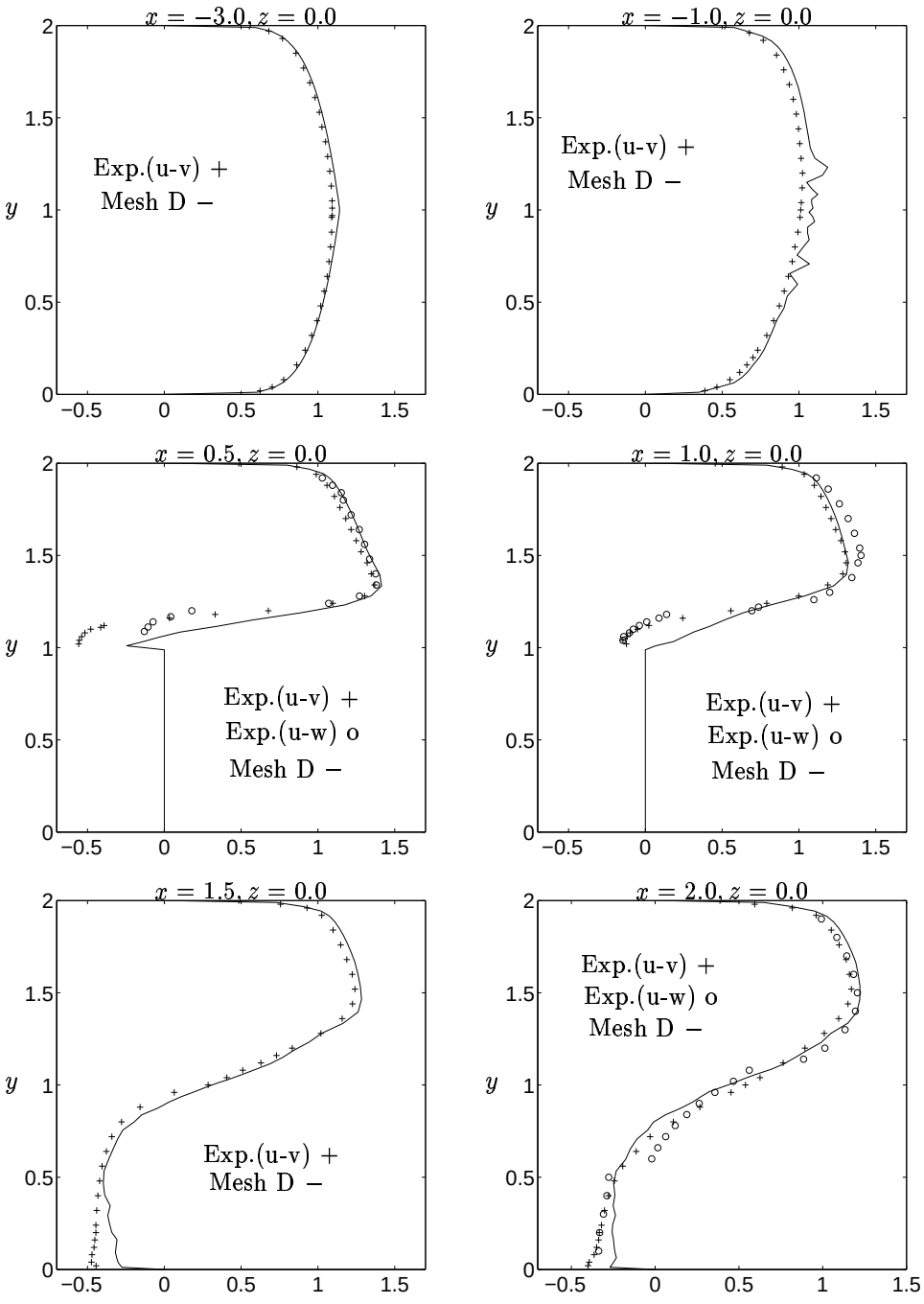

Figure 46: Mean velocity profile $\langle \bar{u} \rangle_t$. Mesh D.

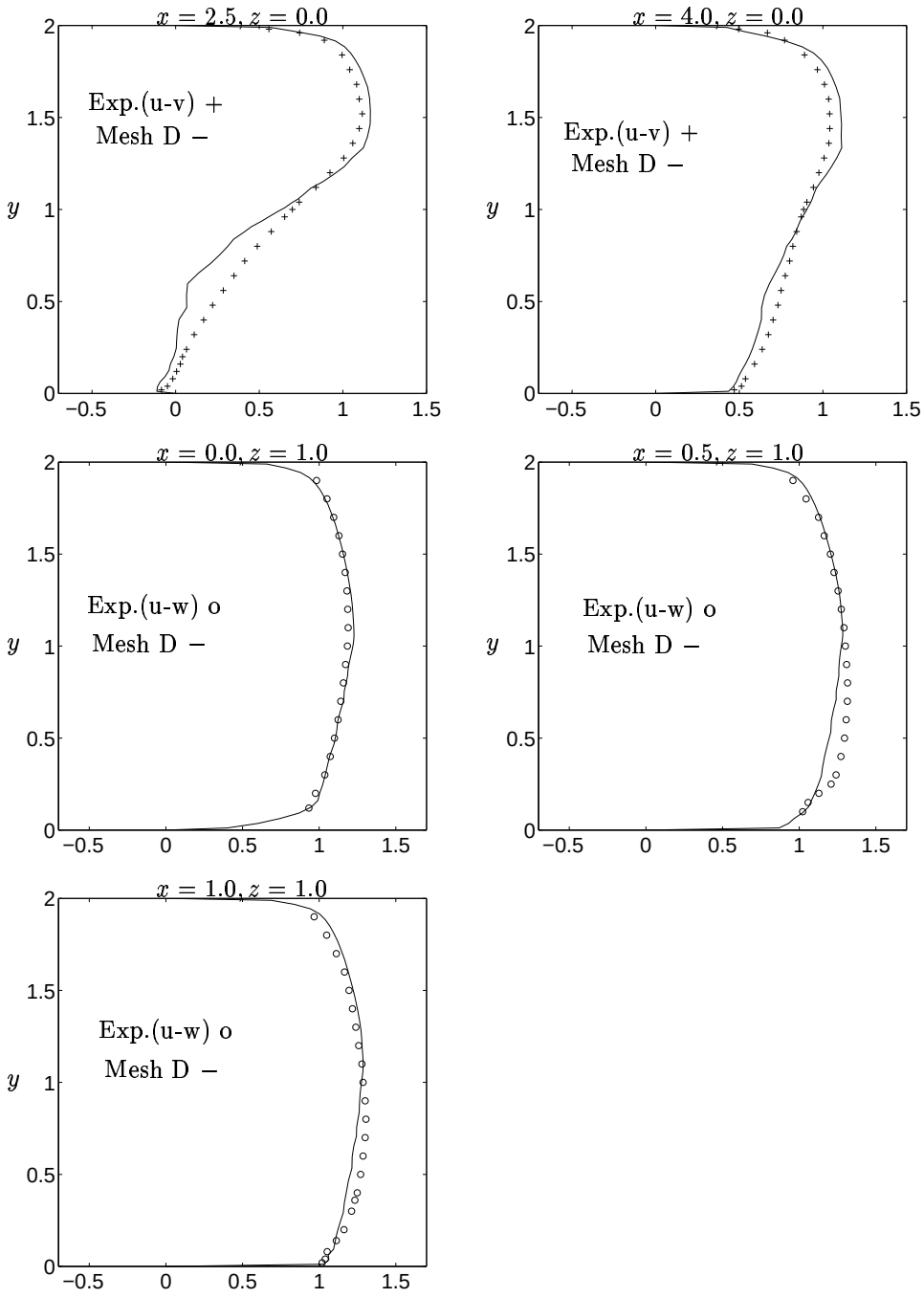

Figure 47: Mean velocity profile $\langle \bar{u} \rangle_t$. Mesh D.

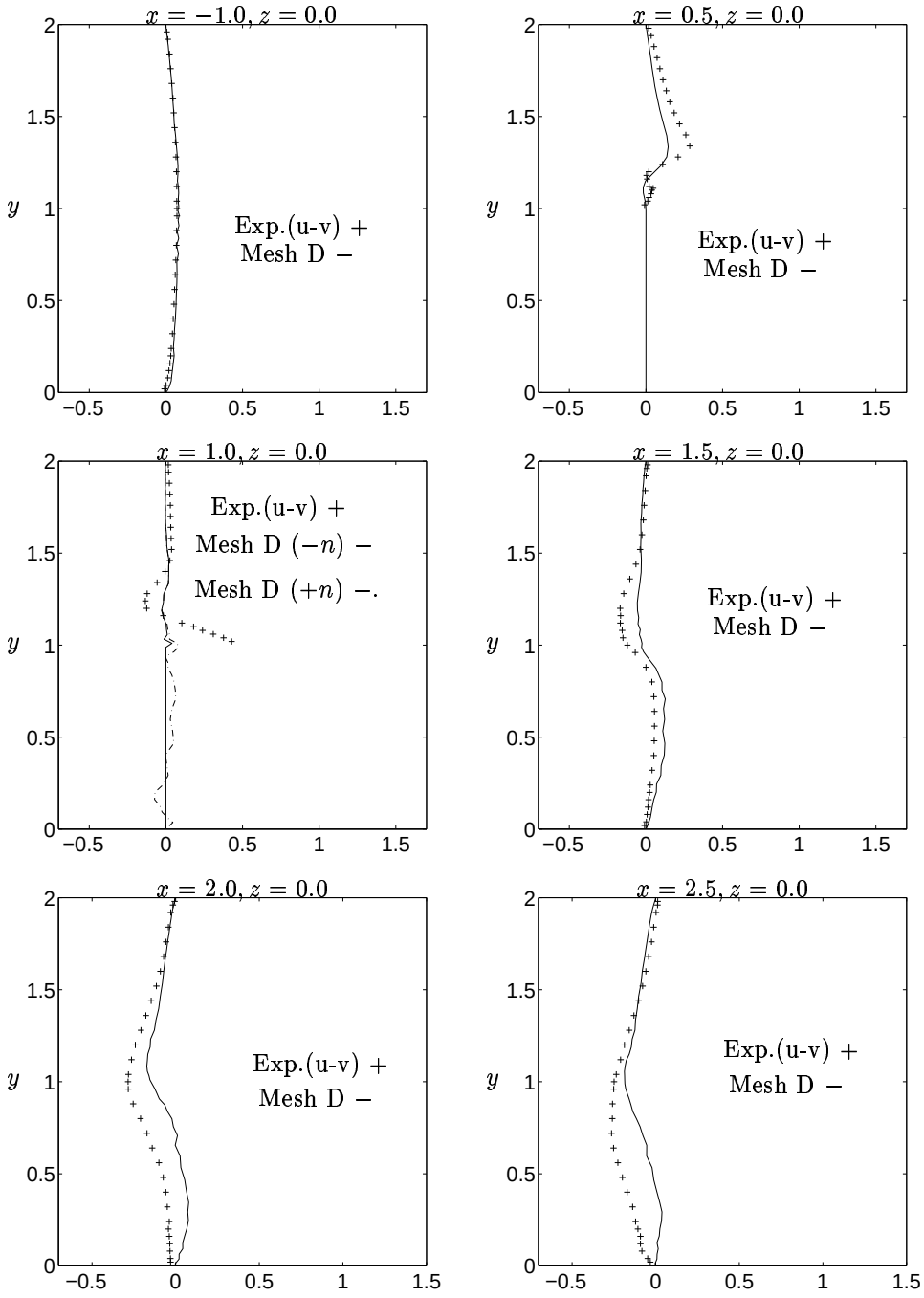

Figure 48: Mean velocity profile $\langle \bar{v} \rangle_t$. Mesh D. In the case $x = 1.0, z = 0.0$ is with $(-n)$ denoted one node before the surface and with $(+n)$ one node after the surface. (In the present work there is no nodes at the surface of the cube!)

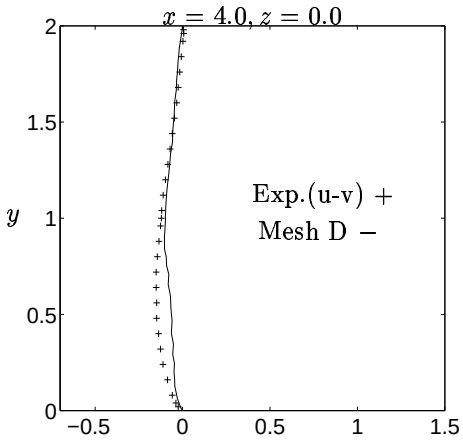

Figure 49: Mean velocity profile $\langle \bar{v} \rangle_t$. Mesh D.

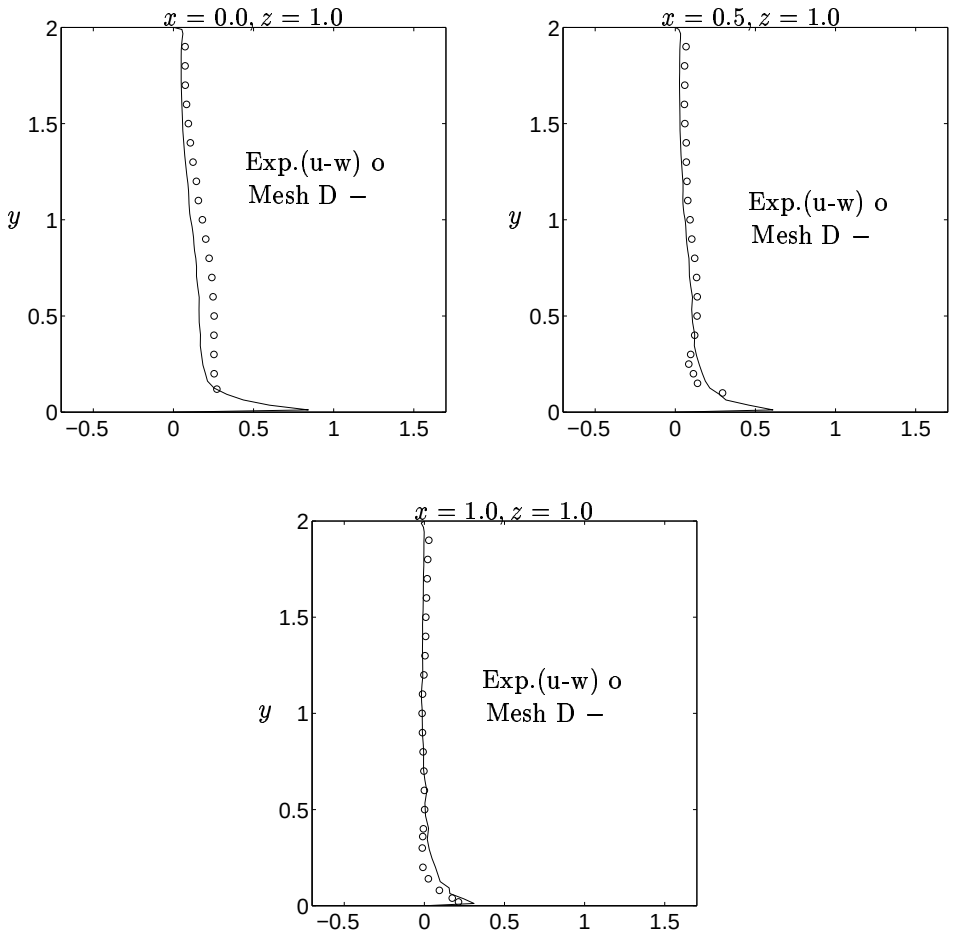

Figure 50: Mean velocity profile $\langle \bar{w} \rangle_t$. Mesh D.

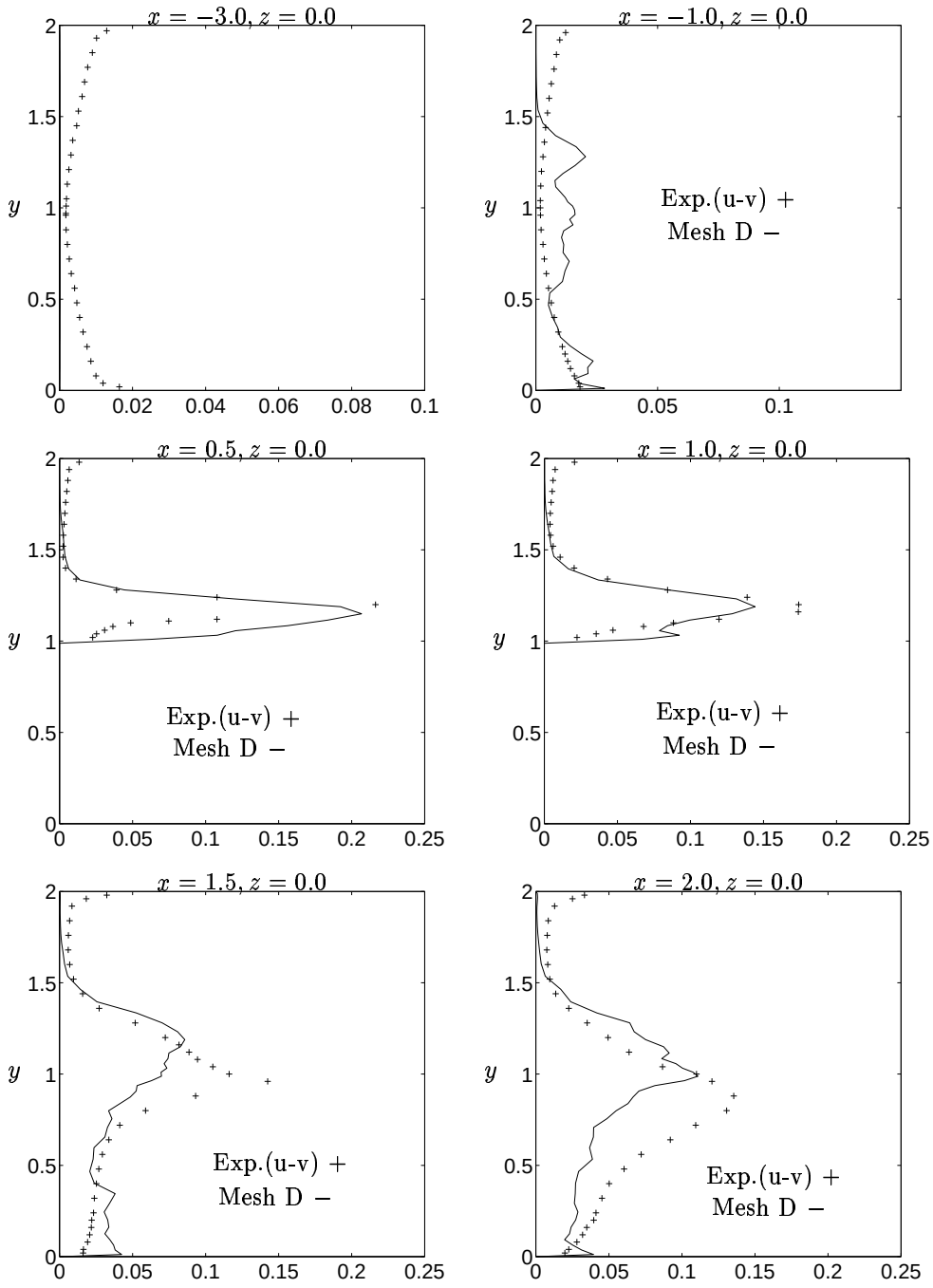

Figure 51: Mean turbulent stress $\langle \overline{u'^2} \rangle_t$. Mesh D.

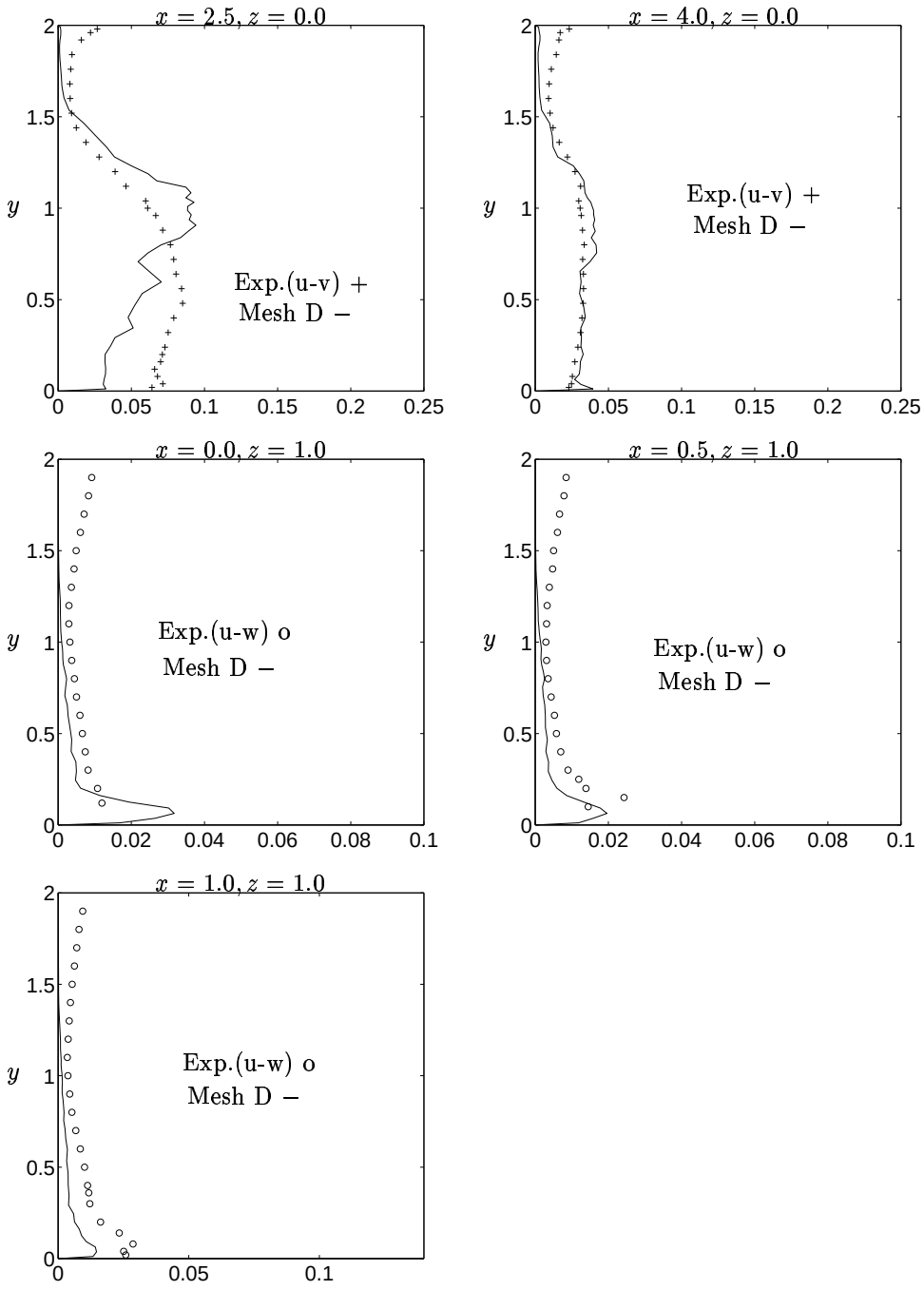

Figure 52: Mean turbulent stress $\langle \overline{u'^2} \rangle_t$. Mesh D.

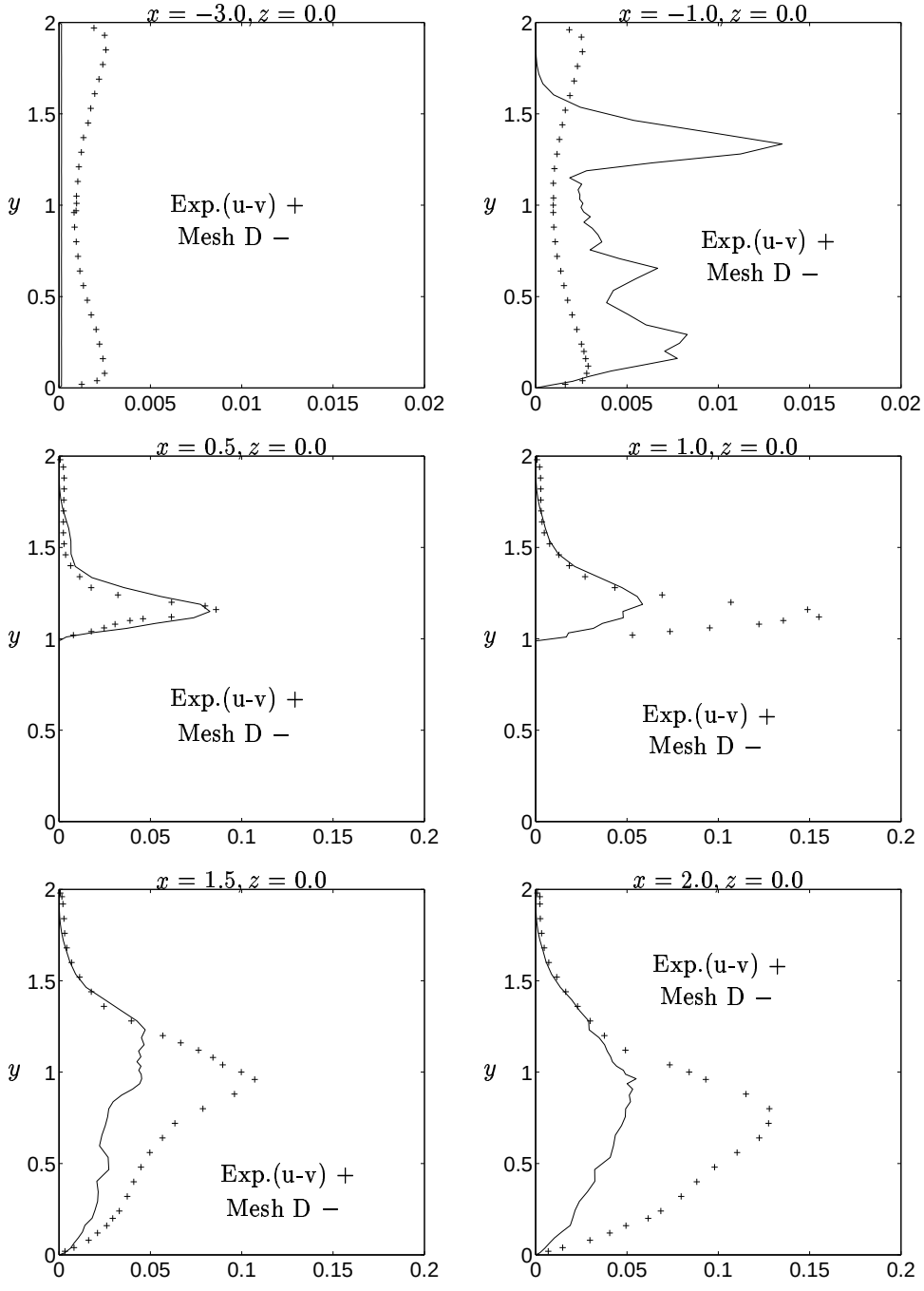

Figure 53: Mean turbulent stress $\langle \overline{v'^2} \rangle_t$. Mesh D.

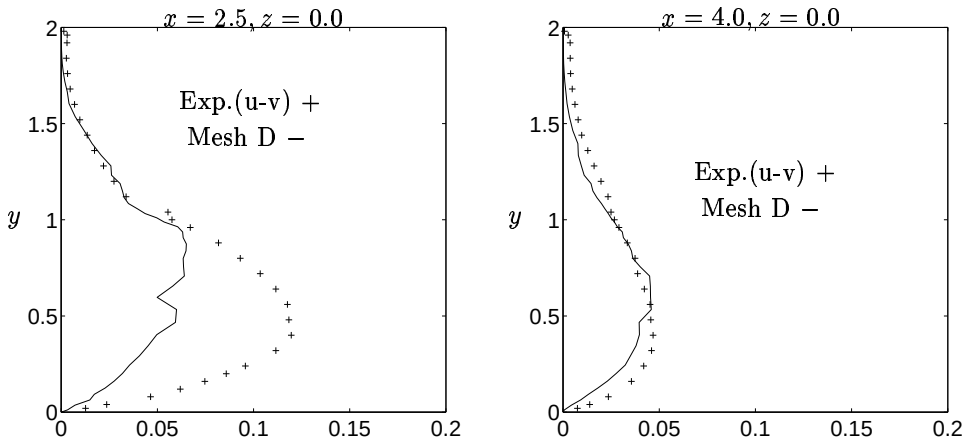

Figure 54: Mean turbulent stress $\langle \overline{v'^2} \rangle_t$. Mesh D.

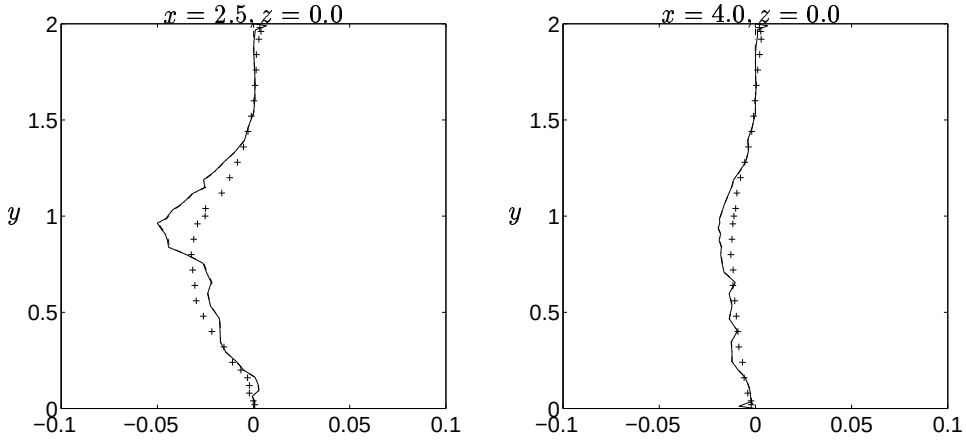

Figure 55: Comparation between resolved mean turbulent stresses $\langle \overline{u'v'} \rangle_t$ $'-.'$ and $\langle \overline{u'v'} \rangle_t + \langle \tau_{12} \rangle_t$ $'-'$. Exp. $(u - v)$ is denoted with $+$. Mesh D.

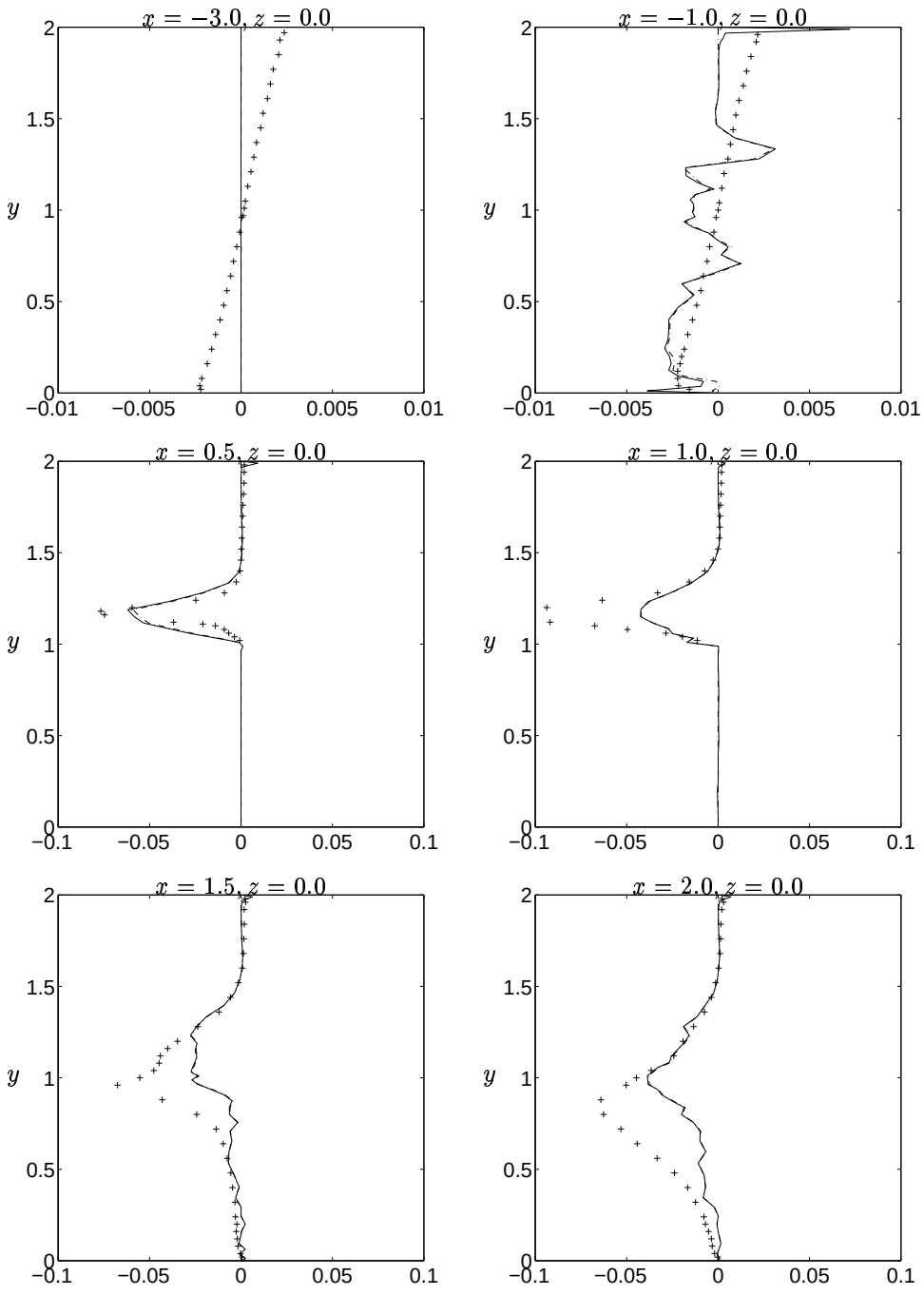

Figure 56: Comparation between resolved mean turbulent stresses $\langle \overline{u'v'} \rangle_t$ $'-.'$ and $\langle \overline{u'v'} \rangle_t + \langle \tau_{12} \rangle_t$ $'-'$. Exp. $(u - v)$ is denoted with $+$. Mesh D.

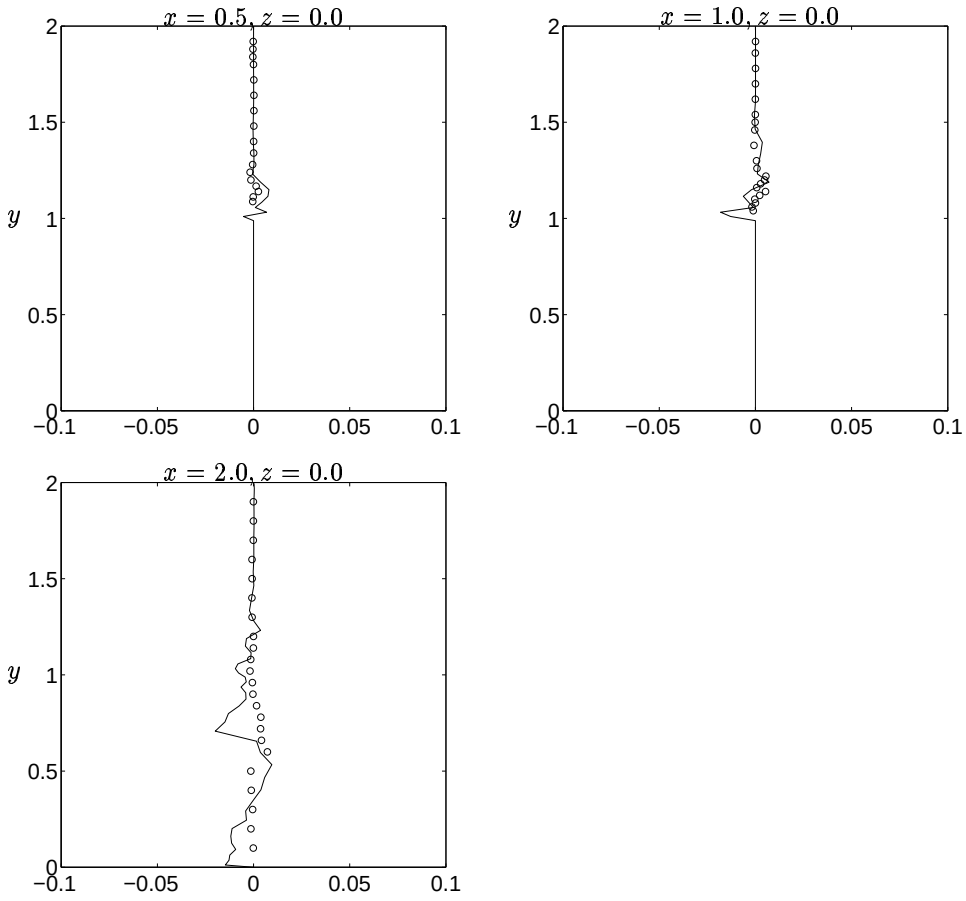

Figure 57: Mean turbulent stress $\langle \overline{u'w'} \rangle_t$ '-'. Exp.$(u - w)$ is denoted with 'o'. Mesh D.

References

[1] A. Leonard. *Energy cascade in large-eddy simulations of turbulent fluid flows* Adv. Geophys., Vol. 18A, pp. 237-248, 1974.

[2] J.W. Deardorff *A numerical study of three-dimensional turbulent channel flow at large Reynolds numbers* Journal of Fluid Mechanics, Vol.41, part 2, pp. 453-480, 1970.

[3] M. Ciofalo. *Large-eddy simulation of turbulent flow and heat transfer: A state of the art rewiew* Dipartimento di Ingegneria Nucleare-Universita di Palermo, Italia, January 1993.

[4] U. Schumann. *Subgrid Scale Model for Finite Difference Simulations of Turbulent Flows in Plane Channels and Annuli.* Journal of Computational Physics 18, pp. 376-404, 1975.

[5] M. Germano, U. Piomelli, . P. Moin, and W. H. Cabot. *A dynamic subgrid-scale eddy viscosity model.* Center for Turbulence Research, Standford, Phys. Fluids A 3(7), July 1991.

[6] W. Rodi, J. H. Ferziger, M. Breuer, and M. Pourquie. *Status of Large Eddy Simulation: Results of a Workshop* Journal of Fluids Engineering, Vol.119, June 1997.

[7] S. Ghosal, T. S. Lund, P. Moin and K. Akselvoll. *A dynamic localisation model for large-eddy simulation of turbulent flows.* Journal of Fluid Mechanics, Vol. 286, pp. 229-255, 1995.

[8] L. Davidson. Large eddy simulations: A note on derivation of the equations for the subgrid turbulent kinetic energies. Rept. 97/11, Dept. of Thermo and Fluid Dynamics, Chalmers University of Technology, Gothenburg, 1997.

[9] L. Davidson. Large eddy simulation: A dynamic one-equation subgrid model for three-dimensional recirculating flow. In *11th Int. Symp. on Turbulent Shear Flow, Grenoble*, volume 3, pp. 26.1–26.6, Grenoble, 1997.

[10] U. Piomelli, and J. R. Chasnov *Large-eddy simulations: Theory and applications.* Turbulence and Transitional modelling, pp. 269-336, 1996 Kluwer Acadsemic Publishers.

[11] W.C. Reynolds *The Potential and Limitations of Direct and Large Eddy Simulations.* Lecture Notes in Physics, Vol. 357, Editor J.L.Lumley, March 22-24, 1989.

[12] R. Martinuzzi, and C. Tropea *The Flow Around Surface-Mounted, Prismatic Obstacles Placed in a Fully Developed Channel Flow.* Journal of Fluids Engineering, pp. 85-91, Vol. 115, March 1993.

[13] A. S. Esfahani *Numerical Study of Laminar, Transitional and Turbulent Flow Past Rectangular Cylinders.* Department of Thermo and Fluid Dynamics, Chalmers University of Technology, 1998.

[14] I. Zacharov *Private communication.* European Supercomputer Team, Silicon Graphics Inc., Switzerland, 1997.